Jefferson Lab PAC 44

Nuclear Exclusive and Semi-inclusive Measurements with a New CLAS12 Low Energy Recoil Tracker

ALERT Run Group†

Executive Summary

In this run group, we propose a comprehensive physics program to investigate the fundamental structure of the ^{4}He nucleus. An important focus of this program is the study of the partonic structure of bound nucleons. To this end, we propose next generation nuclear physics measurements in which low energy recoil nuclei are detected. The tagging of recoiling nuclei especially in deep inelastic reactions will be realized for the first time. This powerful technique will provide unique information about the nature of medium modifications, including the EMC effect, through the measurement of the EMC ratio and its dependence on the nucleon virtuality. Other important channels are the coherent exclusive Deep Virtual Compton Scattering (DVCS) and Deep Virtual Meson Production (DVMP) with a focus on the ϕ meson. These are particularly powerful tools enabling model-independent nuclear 3D tomography through the access of partons' position in the transverse plane. These exclusive measurements will also be used to study the generalized EMC effect and for the first time access the gluonic tomography of nuclei via exclusive ϕ electroproduction channel. Finally, we propose to measure tagged DVCS on light nuclei (d, ^{4}He) to extract both quasi-free neutron and bound neutron and proton Generalized Parton Distributions (GPDs). In both cases, the objective is to study nuclear effects and their manifestation in GPDs including the effect of final state interactions in the measurements of the bound nucleon beam spin asymmetries and the EMC ratio.

At the heart of this program is the Low Energy Recoil Tracker (ALERT) combined with the CLAS12 detector. The ALERT detector is composed of a stereo drift chamber for track reconstruction and an array of scintillators for particle identification. Coupling these two

†Contact Person: Kawtar Hafidi (kawtar@anl.gov)

types of fast detectors will allow ALERT to be included in the trigger for efficient background rejection, while keeping the material budget as low as possible for low energy particle detection. ALERT will be installed inside the solenoid magnet instead of the CLAS12 Silicon Vertex Tracker. We will use an 11 GeV longitudinally polarized electron beam of 150 nA on a gas target straw filled with deuterium or ^{4}He at 3 atm to obtain a luminosity of 2.10^{34} cm^2.s^{-1}. In addition we will need to run hydrogen and ^{4}He targets at different beam energies for detector calibration. The following table summarize our beam time request:

Measurements	**Particles detected**	**Targets**	**Beam time request**	**Luminosity**
ALERT Commissioning	p, ^{4}He	H and He	10 days	2.10^{34} cm^2.s^{-1}
Tagged EMC	p, ^{3}H, ^{3}He	^{2}H and He	$30 + 30$ days	2.10^{34} cm^2.s^{-1}
Tagged DVCS	p, ^{3}H, ^{3}He	^{2}H and He	$30 + 30$ days	2.10^{34} cm^2.s^{-1}
Nuclear GPDs	^{4}He	He	extra 30 days on He	2.10^{34} cm^2.s^{-1}
TOTAL			**100 days**	

Tagged EMC Measurements on Light Nuclei

W.R. Armstrong, K. Hafidi[†], M. Hattawy

Argonne National Laboratory, Lemont, IL 60439, USA

A. Accardi

Hampton University, Hampton, VA 23668, USA

G. Charles[†], R. Dupré[†‡]

Institut de Physique Nucléaire, CNRS-IN2P3, Univ. Paris-Sud, Université Paris-Saclay, 91406 Orsay Cedex, France

M. J. Amaryan, G. Dodge

Old Dominion University, Norfolk, VA 23529, USA

N. Baltzell[†], S. Stepanyan[†]

Thomas Jefferson National Accelerator Facility, Newport News, VA 23606, USA

S. Joosten, Z. E. Meziani, M. Paolone

Temple University, Philadelphia, PA 19122, USA

S. Scopetta

Università di Perugia, INFN, Italy

A. El-Alaoui

Universidad Técnica Federico Santa María, Valparaíso, Chile

S. Liuti

University of Virginia, Charlottesville, VA 22903, USA

[†]Spokesperson

[‡]Contact person: dupre@ipno.in2p3.fr

Abstract

We propose to measure tagged deep inelastic scattering from light nuclei (deuterium and ^{4}He) by detecting the low energy nuclear spectator recoil (p, ^{3}H and ^{3}He) in addition to the scattered electron. The proposed experiment will provide stringent tests leading to clear differentiation between the many models describing the EMC effect, by accessing the bound nucleon virtuality through its initial momentum at the point of interaction. Indeed, conventional nuclear physics explanations of the EMC effect mainly based on Fermi motion and binding effects yield very different predictions for such experiments than more exotic scenarios, where bound nucleons basically loose their identity when embedded in the nuclear medium. By distinguishing events where the interacting nucleon was slow, as described by a mean field scenario, or fast, very likely belonging to a correlated pair, will clearly indicate which phenomenon is relevant to explain the EMC effect. An important challenge for such measurements using nuclear spectators is the control of the theoretical framework and, in particular, final state interactions. This experiment will directly provide the necessary data needed to test our understanding of spectator tagging and final state interactions in ^{2}H and ^{4}He and their impact on the semi-inclusive measurements of the EMC effect described above.

Contents

Introduction

Inclusive electron scattering is a simple and powerful tool to probe the structure of the nucleus, in the Deep Inelastic Scattering (DIS) regime it allows to access the partonic structure of hadrons. Using nucleus as a target permits to study how nucleons and their parton distributions are modified when embedded in the nuclear environment. The modification of quark distributions in bound nucleons was first observed through the modification of the per-nucleon cross section in nuclei, known as the "EMC effect" [1]. For moderate Bjorken x, $0.35 \leqslant x_B \leqslant 0.7$, the per-nucleon DIS structure function for nuclei with A $\geqslant$ 3 was found to be suppressed compared to that of deuterium, the historic measurement being confirmed and refined in the past 30 years [2, 3, 4, 5, 6, 7].

Since its discovery, the EMC effect has been a subject of extensive theoretical investigations aimed at understanding its underlying physics. While progress has been made in interpreting the main features of the effect, no single model has been able to explain convincingly the effect for both its x_B and A dependencies [8, 9, 10]. A unifying understanding of the physical picture is still under intense debate. Most models of the EMC effect can be classified into two main categories:

- "Conventional" nuclear models [11, 12, 13, 14] in which the effect could be understood by a reduced effective nucleon mass in the nuclear potential, causing a shift of x_B to higher values (x_B-rescaling or binding models). In these models the mass shift is sometimes accompanied by an increased density of virtual pions associated with the nuclear force (pion cloud models).

- Models involving the change of the quark confinement size in the nuclear medium [15, 16, 17, 18] can be viewed, in the language of QCD, as Q^2 rescaling models. In some cases a simple increase of the nucleon radius is assumed (nucleon swelling), while in others quark deconfinement is invoked and the nucleon degrees of freedom are replaced by multi-quark clusters.

- Some more elaborate models fall in between or give very different predictions. We note here in particular the Point Like Configurations (PLC) suppression model as it gives direct predictions as a function of the nucleon virtuality. It was argued in [19] that PLCs are suppressed in bound nucleons and that large x_B configurations in nucleons have smaller than average size leading to the EMC effect at large x_B. The EMC effect

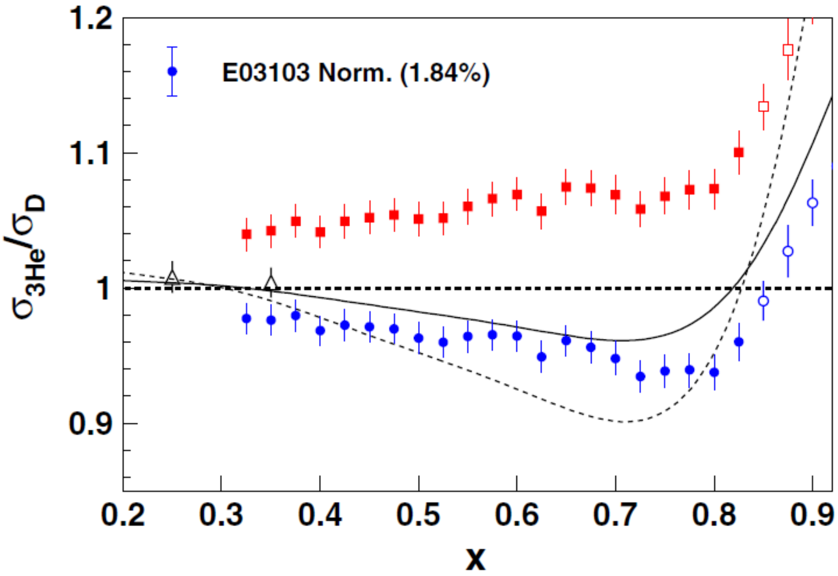

Figure 1: EMC ratio ^{3}He, the upper squares are the raw ^{3}He/^{2}H ratios, while the bottom circles show the isoscalar EMC ratio. The triangles are the HERMES results [20] which use a different isoscalar correction. The solid and dashed curves are the SLAC A-dependent fits to ^{3}He and carbon, respectively [7].

in this model is predicted to be proportional to the off shellness of the stuck nucleon and hence dominated by the contribution of the short-range correlations.

Recent experiment at Jefferson Lab measured the EMC effect for a series of light nuclei [7]. Fig. 1 shows the first measurements of the EMC effect for ^{3}He at large x_B. It is found to be roughly one third of the effect observed in ^{4}He, violating the A-dependent fit to the SLAC data, in the same way, the large EMC effect found in ^{9}Be contradicts a simple density-dependent behavior (Fig. 2). This suggests that the EMC effect may be sensitive to the local density or details of the nuclear structure, which has been first introduced in [21], some models have predicted a local EMC effect and describe the modification of the nucleons depending on their shells [22, 23, 24]. The possibility of the EMC effect depending on the local environment of the nucleon also motivates the investigation of possible connections between the EMC effect and other density-dependent effects such as short range correlations [25, 26].

Short range correlations (SRC) occur between nucleons located at less than the average inter-nucleon distance with high relative momentum [27, 28, 29]. Those pairs of nucleons carry 80% of all nucleons kinetic energy inside the nucleus although they only represent about 20% of the nucleons [30]. The plateau obtained in the inclusive cross section ratios of two nuclei (for example iron and deuterium) in the region $x_B > 1.5$ for $Q^2 > 1.5$ GeV^2 indicates that for nucleon momentum larger than Fermi momentum ($p \geqslant p_N \simeq 275$ MeV/c), the nucleon momentum distributions in different nuclei have similar shapes but differ in

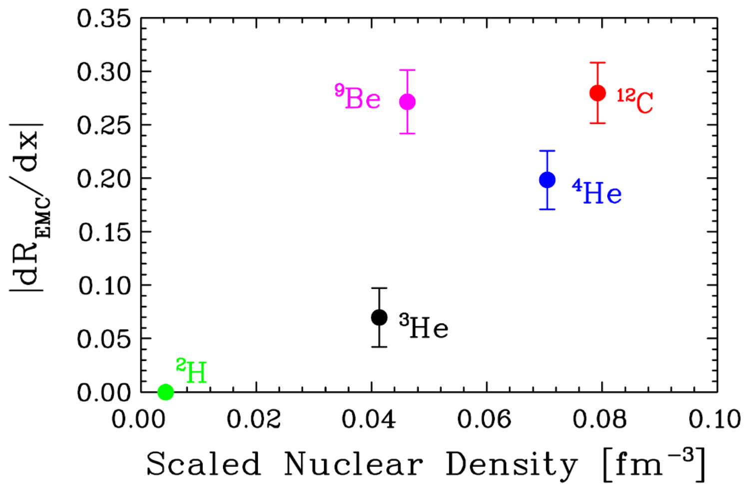

Figure 2: The slope of the isoscalar EMC ratio for $0.35 < x_B < 0.7$ as a function of nuclear density [7].

magnitude. The ratio of the cross sections in the plateau region also called the "SRC scale factor $a_{2N}(A/d)$" was found to be linearly correlated with the slope of the EMC effect [26]. This striking correlation shown in Fig. 3 could indicate that high momentum bound nucleons are important players in the EMC effect.

To investigate the matter further, it is important to study the EMC effect as a function of both x_B and the nucleon virtuality, by measuring the recoil fragment in addition to the scattered electron as is developed in this proposal (the relation between spectator momentum and virtuality has been studied in detail in [31]). The two main challenges to perform such a measurement are, first, to be able to detect the low energy nuclear fragments and, second, to understand the Final State Interaction (FSI) effects on the observables.

The recent development of two small radial time projection chambers (RTPC) by the CLAS collaboration for the measurement of the structure function of the neutron, by tagging the spectator proton from a deuterium target [32], and the measurement of coherent deep virtual Compton scattering off ^{4}He [33] has raised a lot of interest to use a RTPC for this proposed tagged EMC measurement. However, it was found that the particle identification capabilities of the RTPC are not good enough to properly differentiate the different nuclear isotopes measured (in particular ^{3}H from ^{3}He). Therefore, we propose to use a different detector based on a low gain drift chamber and a scintillator array for time of flight measurement. Such detector appears to be perfectly suited for our measurement as it offers low energy and large angle capabilities to measure slow recoils similar to the RTPC. Moreover, such detector will be much faster to collect the deposited charges making it possible to include it in the trigger. This will allow to reject the overwhelming majority of the events ($\sim 90\%$) where the nuclear recoil does not make it into the detection area.

Another important issue for tagged measurements is to control the impact of FSI on the

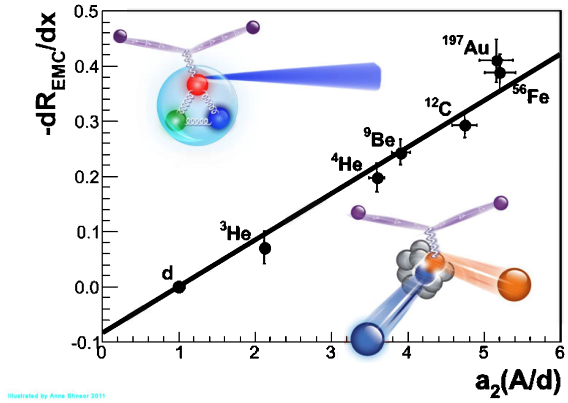

Figure 3: The EMC slopes versus the SRC scale factors. The uncertainties include both statistical and systematic errors added in quadrature.

observables. The large acceptance of both CLAS12 and ALERT is very important in this regard as it allows to measure at the same time the regions of the phase space expected to have low FSI and the regions where we expect more. The models used to correct for FSI [34, 35, 36, 37] can therefore be tested on a wide kinematic range in the exact same conditions as the main measurement in order to make sure that the effect is understood properly. Then with the application of cuts to select the region where the effect is smaller, we can reduce the impact of FSI to a minimum. This procedure allows to make sure FSI effects are small and under control to minimize systematic uncertainty on our observables.

Chapter 1

The EMC effect in SIDIS

At this point, it became clear that in order to advance our understanding of the EMC effect, it is necessary to study new observables such as the nucleon virtuality which can be accessible in semi inclusive measurements. Interests for slow nucleons and fragments tagging ($e+A \to e'+N+X$) studies are older than the EMC effect itself and has been identified earlier to be a promising tool to study nuclear effects [21, 38, 39]. In more recent work, Melnitchouk *et al.* [40] showed that the tagged structure functions of deuteron in $(e, e'N_s)$ semi-inclusive reactions, where N_s denotes the spectator nucleon, is a sensitive probe of the modification of the intrinsic structure of the bound nucleon allowing to discriminate between different EMC models. The extended case to heavier nuclei A, where the recoil nucleus $(A-1)$ is tagged was developed by Ciofi degli Atti *et al.* [24, 37, 41, 42], demonstrating the importance of such measurements in the understanding the EMC-type effects. In this proposal, we would like to test experimentally the validity of the spectator mechanism and investigate the origin of the medium induced modification of the nucleon structure function through several observables based on tagged DIS off deuterium and helium targets.

1.1 The spectator mechanism

In the spectator mechanism or plane wave impulse approximation (PWIA), the DIS process corresponds to the absorption of the virtual photon by a quark inside a nucleon, followed by the recoil of the spectator nucleus $A-1$ with low recoil momentum ($\vec{P}_{A-1}$) and low excitation energy (Fig. 1.1). The differential semi-inclusive cross section can be written as [24]

$$\sigma_1^A(x_B, Q^2, \vec{P}_{A-1}, y_A, z_1^A) = \frac{d^4\sigma}{dx dQ^2 d\vec{P}_{A-1}} = K^A(x, y_A, Q^2, z_1^A) n_A(|\vec{P}_{A-1}|) z_1^A F_2^{N/A}(x_A, Q^2, p_1^2), \tag{1.1}$$

where $Q^2 = -q^2 = -(k_e - k_e')^2 = \vec{q}^{\,2} - \nu$ is the four-momentum transfer, with $\vec{q} = \vec{k_e} - \vec{k_e'}$ and $\nu = E_e - E_e'$, $x_B = Q^2/2M\nu$ is the Bjorken scaling variable, $p_1 \equiv (p_{10}, \vec{p_1})$, with $\vec{p_1} \equiv -\vec{P}_{A-1}$,

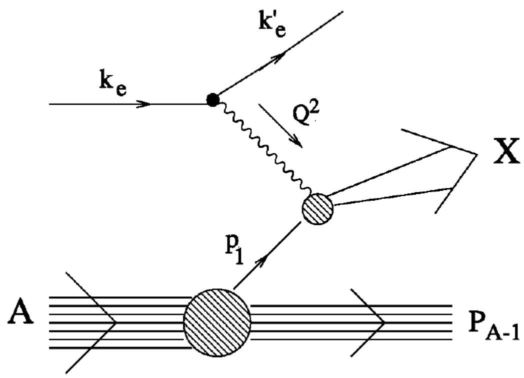

Figure 1.1: The process $A(e, e'(A-1))X$ within the impulse approximation [24].

is the four-momentum of the nucleon before its interaction with the virtual photon. $F_2^{N/A}$ is the DIS structure function of the nucleon N in the nucleus A, $n_A(|\vec{P}_{A-1}|)$ is the three-momentum distribution of the bound nucleon, $z_1^A = (p_1 \cdot q)/M\nu$ is the light cone momentum fraction of the struck quark and K^A is a kinematical factor given by

$$K^A(x_B, y_A, Q^2, z_1^A) = \frac{4\pi\alpha^2}{Q^4 x_B} \cdot \left(\frac{y}{y_A}\right)^2 \times \left(\frac{y_A^2}{2} + (1-y_A) - \frac{p_1^2 x_B^2 y_A^2}{(z_1^A)^2 Q^2}\right), \tag{1.2}$$

with $y = \nu/E_e$, $y_A = (p_1 \cdot q)/(p_1 \cdot k_e)$ and $x_A = x_B/z_1^A$.

Nuclear effects in Eq. 1.1 are generated by the nucleon momentum distribution $n_A(|\vec{P}_{A-1}|)$ and by the quantities y_A and z_1^A, which differ from the corresponding quantities for a free nucleon ($y = \nu/E_e$ and $z_1^N = 1$). In this framework the off-mass shellness of the nucleon ($p_1^2 \neq M^2$) generated by nuclear binding is taken into account within some small relativistic corrections when $A > 2$ [43]. In all the studies we propose here, as well as in proposals such as [44, 45, 46], it is important to insure that the spectator mechanism is working and that rescattering with spectator nucleons is properly modeled. Our main goal here is to make sure we understand deuterium and the extension of the formalism to the helium target.

To test the spectator mechanism, we use the $\vec{P}_{A-1}$ dependence of semi-inclusive cross section ratio of different nuclei at the same values of x_B, Q^2 and with $|\vec{P}_{A'-1}| = |\vec{P}_{A-1}|$

$$R(x_B, Q^2, |\vec{P}_{A-1}|, z_1^A, z_1^{A'}, y_A, y_{A'}) \equiv \frac{\sigma_1^A(x_B, Q^2, |\vec{P}_{A-1}|, z_1^A, y_A)}{\sigma_1^{A'}(x_B, Q^2, |\vec{P}_{A'-1}|, z_1^{A'}, y_{A'})}. \tag{1.3}$$

In the Bjorken limit, the A dependence of R is expected to be entirely dominated by the A dependence of the nucleon momentum distribution $n_A(|\vec{P}_{A-1}|)$, which exhibits a strong A dependence at low recoil momentum region. Therefore, measurements of the R ratio as a function of the recoil momentum $|\vec{P}_{A-1}|$ provides a stringent test for the spectator mechanism

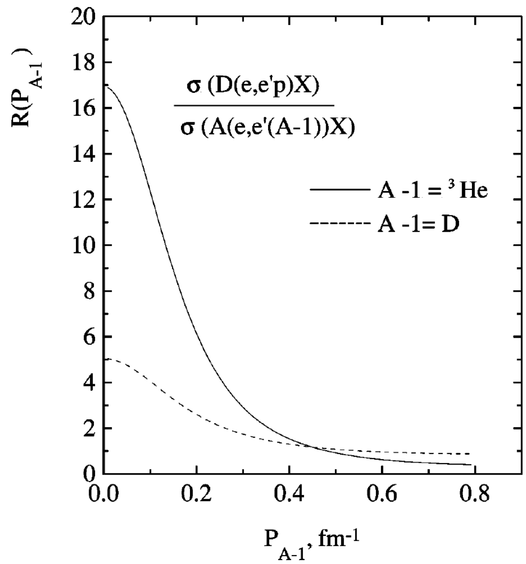

Figure 1.2: The ratio $R(A, A', |\vec{P}_{A-1}|)$ for the targets ^{3}H (dashed) and ^{4}He (full) as a function of the momentum of the backward emitted nucleus [24] relative to the virtual photon direction.

independently of the model for $F_2^{N/A}$. Fig. 1.2 illustrates the expected behavior of the ratio in Eq. 1.3 from the processes D$(e, e'p)X$, ^{3}He$(e, e'$D$)X$ and ^{4}He$(e, e'^3$He$)X$, as deep inelastic scattering from a bound neutron in different nuclei.

From the previous discussion, it is clear that the observation of recoiling nuclei in the ground state, with a $|\vec{P}_{A-1}|$-dependence similar to the one predicted by the momentum distributions, would represent a stringent check of the spectator mechanism, which, in turns, would indicate the absence of significant Final State Interaction (FSI) between the electroproduced hadronic states and the nuclear medium. Detailed studies [34, 35, 36, 37, 40, 47] have shown that the FSI effects are minimized in the backward recoiling angle relative to the virtual photon direction and maximized in perpendicular kinematics. The detection of the ground or low energy excited states of the $(A-1)$ recoil would represent a strong indication that the hadronization length is larger than the effective nuclear dimension, since if the struck quark hadronizes inside the nucleus, it will likely result in its breakup.

1.2 EMC effect in deuterium

The recent finding of the possible dependence of the EMC effect on the local density increased the interest in using spectator nucleons to study the EMC effect. Indeed, the momentum of the spectator nucleon is directly linked to the distance between the two nucleons of deuterium [43].

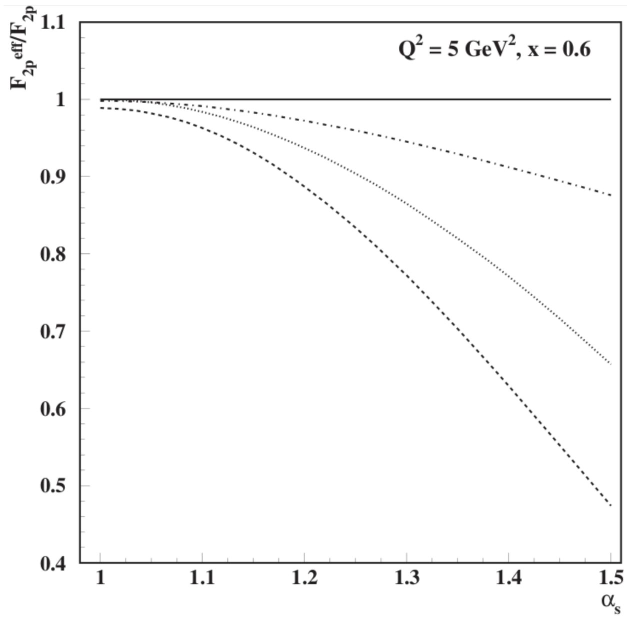

Figure 1.3: F_{2p}^{eff} as a function of α_s for $x = 0.6$ and $p_T = 0$. Dashed line is a prediction for the PLC suppression model, dotted is for the Q^2-rescaling model, and dot-dashed for the binding/off-shell model [40].

Melnitchouk *et al.* [40] use the ratio of the effective F_{2p}^{eff} measured in the deuterium, tagging the neutron, and compare it to the usual free F_{2p}. They predict significant effects for various models as a function of $\alpha \equiv \dfrac{E_s - p_z^s}{M}$ (with E_s and p_z^s the energy and longitudinal momentum of the spectator, respectively, and M its mass), which characterizes the nucleon virtuality. A semi-inclusive measurement will allow to discriminate between the very different model predictions (Fig. 1.3).

1.3 EMC effect in helium

The process described for deuterium can be easily extended to heavier nuclei with several advantages. First, the nuclear effects in light nuclei, such as ^{4}He, are much stronger, thus it enhances significantly the cross section for events with spectator momentum $\gtrsim$ 250 MeV. Second, by detecting an intact light nucleus (^{3}H or ^{3}He), we ensure that the final state interaction with the spectator is small and the contributions from the current or target fragmentation of the hard process are suppressed. On the down side, the theoretical calculations are more difficult, however recent theoretical progress indicates that these calculations although tedious could be performed [34, 36, 37, 39, 43].

The quantity R^A which is defined by:

$$R^A(x_B, x'_B, Q^2, |\vec{P}_{A-1}|) \equiv \frac{\sigma_1^A(x_B, Q^2, |\vec{P}_{A-1}|, z_1^{(A)}, y_A)}{\sigma_1^A(x'_B, Q^2, |\vec{P}_{A-1}|, z_1^{(A)}, y_A)}, \tag{1.4}$$

represents the ratio between the cross sections on the nucleus A at two different values of the Bjorken scaling variable. Due to the cancellation of all the other terms but the nucleon structure functions in Eq. 1.4, R^A is highly sensitive to the nuclear effect. In the binding model (x-rescaling), where the inclusive nuclear structure function is expressed through a convolution of the nuclear spectral function and the structure function of the bound nucleon, one has

$$R^A(x_B, x'_B, Q^2, |\vec{P}_{A-1}|) = \frac{x'_B}{x_B}\frac{F_2^{N/A}(\frac{x_B}{z_1^A}, Q^2)}{F_2^{N/A}(\frac{x'_B}{z_1^A}, Q^2)}. \tag{1.5}$$

In the Q^2-rescaling model [18], which is based on the medium modification of the Q^2-evolution equations of QCD and the assumption that the quark confinement radius for a bound nucleon is larger than for a free one, the ratio becomes

$$R^A(x_B, x'_B, Q^2, |\vec{P}_{A-1}|) = \frac{x'_B}{x_B}\frac{F_2^{N/A}(x_B, \xi_A(Q^2)Q^2)}{F_2^{N/A}(x'_B, \xi_A(Q^2)Q^2)} \tag{1.6}$$

While Eq. 1.5 is expected to depend both on A and $|\vec{P}_{A-1}|$, Eq. 1.6 would be a constant. By detecting nuclei with different recoil angles, this ratio would exhibit different behaviors, allowing a more detailed examination of the dynamics. Fig. 1.4 shows theoretical predictions of the R^A ratio in the x- and Q^2-rescaling models at both perpendicular and backward recoil kinematics.

1.4 Tagged EMC ratio

Another observable used in theoretical calculations for the tagged EMC ratio is

$$R_0(x, Q^2) = \frac{\int_a^b \sigma_1^A d\vec{P}_{A-1}}{\int_a^b \sigma_1^D d\vec{P}_{A-1}}, \tag{1.7}$$

in which the cross section is integrated over a small momentum range of the recoil nucleus $\vec{P}_{A-1}$. In binding models it leads to opposite behavior for recoil nuclei emitted forward versus backward (Fig. 1.5) that cancels in the usual EMC effect. This leads to deviations much larger than the usual inclusive EMC effect and provides opportunity for a significant experimental check of the binding models.

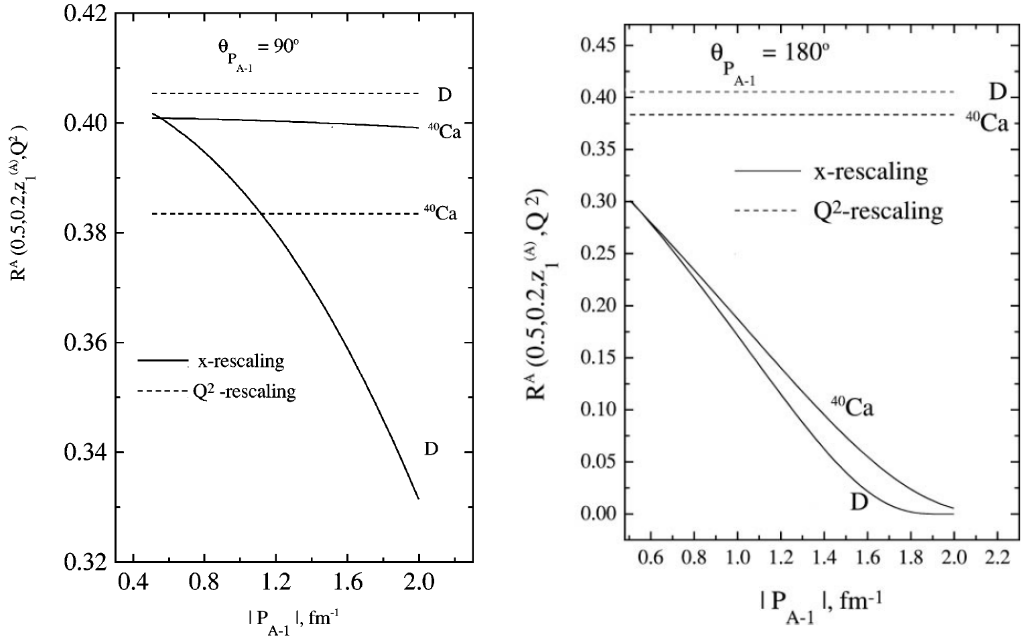

Figure 1.4: The ratio $R^A(x_B, x'_B)$ for $A = 2$ and $A = 40$, $x_B = 0.2$ and $x'_B = 0.5$, $Q^2 = 20$ GeV/c, plotted versus the momentum of the recoil nucleus $(A - 1)$ at perpendicular (left) and backward (right) angle ($\theta_{P_{A-1}} = 180°$). The full and dashed curves are predictions of the x_B-rescaling (binding) and Q^2-rescaling models, respectively.

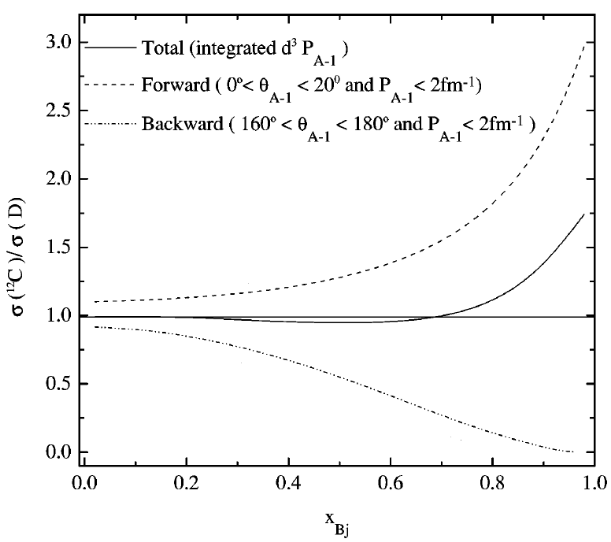

Figure 1.5: The semi-inclusive EMC ratio $R_0(x, Q^2)$ versus x with nuclei emitted forward and backward, the full curve is the usual inclusive EMC ratio, the dashed and dotted curves are predictions for the local EMC effect for different spectator recoil angles [24] (see the legend).

1.5 Flavor dependent parton distribution functions

Measurements of tagged structure functions have been carried in CLAS by the e6 run group to study the EMC effect in deuteron [47] and later by the BoNuS collaboration [48] to extract the F_2^n structure function by tagging the low momentum recoil proton. The main goal of the BoNuS measurements is to extract the ratio F_2^n/F_2^p at high x_B and therefore access the ratio of down to up quark distribution (d/u) [32]. By using ^{4}He targets and tagging the recoiling ^{3}He and ^{3}H nuclei, one can select scattering off a weakly or deeply bound neutron and proton respectively depending on their off-shellness in the ^{4}He nucleus. Since bound neutrons are always off-shell, even when $P_{^3He} = 0$, an extrapolation procedure is needed to extract the free (i.e. on-shell) neutron structure function from the tagged recoil data [49, 50]. One could measure the F_2 structure functions of a weakly bound neutron in ^{4}He and compare it to the ^{2}H data to detect any nuclear dependence. This procedure is necessary for neutrons due to the absence of a free neutron target. It can also be quantitatively benchmarked using the ^{4}He tagged data for scattering off a weakly bound proton, and comparing the results to the well measured free proton structure functions.

In addition, the ratio $(F_2^n/F_2^p)^{bound} / (F_2^n/F_2^p)^{free}$ can be measured to extract the distributions of d/u in a free nucleon and compare it to the same ratio for bound nucleon. This is one of the way to explore the flavor dependent nuclear parton distributions which are little known experimentally. Such an effect, either in the antishadowing or EMC region, has been widely used to explain the NuTeV anomaly [51, 52].

1.6 Summary

In this chapter, we have shown very strong theoretical incentives to measure the tagged structure function of nucleons in light nuclei such as deuterium and helium. The main difficulty being to properly handle the FSI, to solve this a large acceptance detector is necessary in order to demonstrate that data match models on a wide kinematic range in angle and momentum. Moreover, such large acceptance detector need to work at the lowest possible energy to ensure that quasi-free nucleons of low virtuality can be effectively compared with the more virtual ones. Our proposition for such a detector is presented in the next chapter.

We presented theoretical work suggesting that a measurement on deuterium will already show an effect, however we also showed that higher nuclear masses provide much stronger signals and would insure a compelling measurement. Observing several nuclei in different kinematics lead to very different results for the classic pure x_{Bj} and Q^2-rescaling models. This will allow us to determine precisely which picture or which combination of the two pictures is at the origin of the EMC effect. This measurement will therefore provide a completely new insight into the origin of the EMC effect and provide clear guidelines to build new models and better understand the partonic structure of nuclei.

In addition, our proposed experiment is able to test the flavor symmetry of the nuclear effects, which have been discussed by theoretical predictions in the anti-shadowing and EMC regions. While this experiment is not dedicated to this question, for which additional isospin asymmetric targets would be necessary, we show that it can already provide a first test and pave the way for future works.

Chapter 2

Experimental Setup

The different measurements of the ALERT run group require large kinematic coverage and the ability to identify the different nuclear spices properly. The CLAS12 detector augmented by an adapted low energy recoil detector is key for the success of such measurements. We summarize in table 2.1 the requirements for the different experiments proposed in the run group.

Measurement	Particles detected	$p_{threshold}$	θ_{max}
Tagged EMC	p, ^{3}H, ^{3}He	As low as possible	As close to π as possible
Tagged DVCS	p, ^{3}H, ^{3}He	As low as possible	As close to π as possible
Nuclear GPDs	^{4}He	$230 < p < 400 MeV/c$	$\pi/4 < \theta < \pi/2$ rad

Table 2.1: Requirements for low momentum spectators fragments of the measurements proposed.

2.1 CLAS12 Forward Detector

The CLAS12 detector is designed to operate with 11 GeV beam at an electron-nucleon luminosity of $L = 1 \times 10^{35}$ cm^{-2}s^{-1}. The baseline configuration of the CLAS12 detector consists of the Forward Detector and the Central Detector packages [53] (see Fig. 2.1).

The scattered electrons will be detected in the forward detector which consists of the High Threshold Cherenkov Counters (HTCC), Drift Chambers (DC), the Low Threshold Cherenkov Counters (LTCC), the Time-of-Flight scintillators (TOF), the Forward Calorimeter and the Preshower Calorimeter. The charged particle identification in the forward detector is achieved by utilizing the combination of the HTCC, LTCC and TOF arrays with the tracking information from the Drift Chambers. The HTCC together with the Forward Calorimeter and the Preshower Calorimeter will provide a pion rejection factor of more than 2000 up to a momentum of 4.9 GeV/c, and a rejection factor of 100 above 4.9 GeV/c.

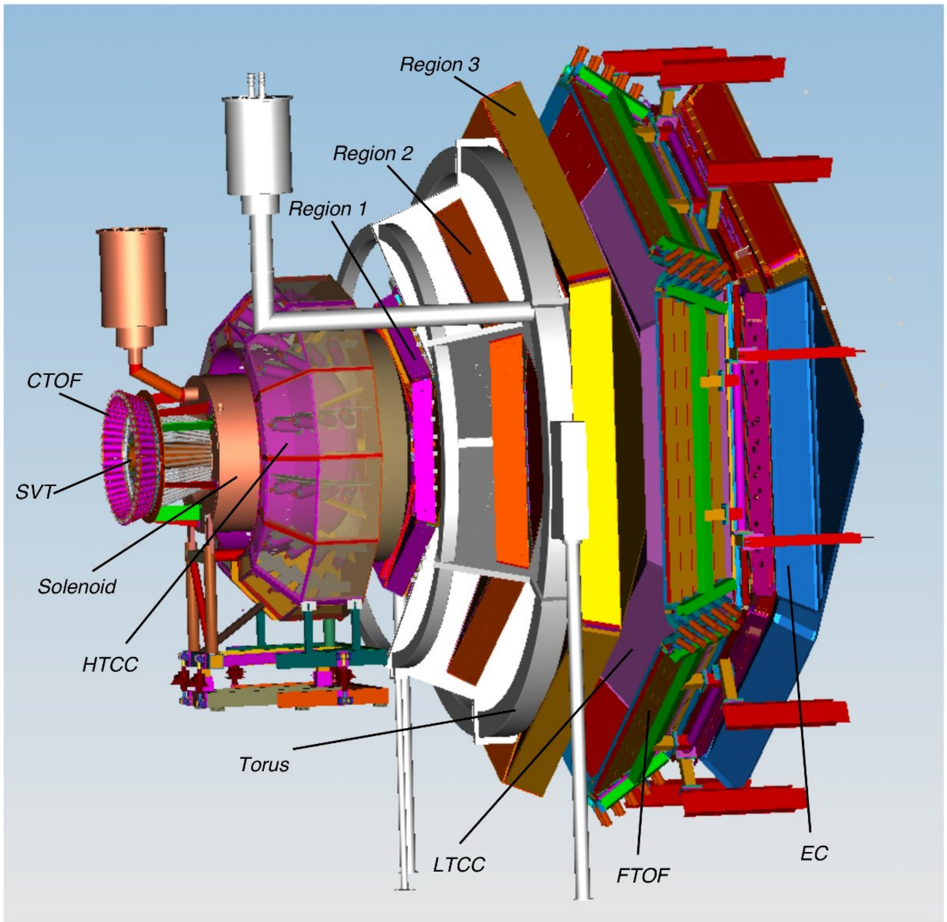

Figure 2.1: The schematic layout of the CLAS12 baseline design. In the proposed measurements CLAS12 forward detectors will be used to measure the electrons.

2.2 Design of ALERT Detector

We propose to build a low energy recoil detector consisting of two sub-detectors systems: a drift chamber and a scintillator hodoscope. The drift chamber will be composed of 8 layers of sense wires to provide track information while the scintillators will primarily provide particle identification. To reduce the material budget, thereby lowering the energy threshold for detecting low energy recoil particles, the scintillator hodoscope will be placed inside the chamber, just outside of the last layer of drift wires. The good time resolution, and therefore position resolution, of the drift chamber coupled with the scintillators will provide energy loss, timing, and azimuthal angle for a large domain of particles and energy.

The drift chamber will be filled with a light gas mixture such as He(90%) and C_4H_{10}(10%) to not be sensitive to relativistic particles (*i.e.* electrons, gammas) and neutron backgrounds. A light gas mixture also increases the drift speed of electrons created during the ionization, which allows the chamber to withstand a higher particle rate. The gas will likely be at atmospheric pressure but we plan on evaluating the possibility of working at a lower pressure. Based on these characteristics, the signals from this chamber and the scintillators will be used as an independent trigger, thus, reducing the DAQ frequency allowing operation at increased luminosity.

The detector must be designed to fit inside the outermost layer of Micromegas; the silicon vertex tracker and the other layers of Micromegas will be removed. The available space has thus an outer radius of 200 mm. A schematic layout of the preliminary design is shown in Fig. 2.2. The different detection elements are all covering about 340° of the polar angle to leave room for mechanics, and are 300 mm long with an effort made to reduce the particle energy loss through the materials. It is composed of:

- a cylindrical target, that compared to the EG6 run, is longer ($\sim$30 cm), wider (outer radius is 6 mm) and operating with lower pressure ($\sim$3 atm) in order to use a thinner target wall ($\sim$25μm Kapton) [1];
- a clear space filled with helium to reduce secondary scattering from the high rate Moller electrons. Its outer radius is 30 mm;
- the drift chamber, its inner radius is 32 mm and its outer radius is 85 mm. It will detect the trajectory of the low energy nuclear recoil;
- two rings of plastic scintillators placed inside the gaseous chamber, with total thickness of roughly 20 mm.

[1] During the EG6 run, the pressure of the drift gas in the RTPC was $\sim$1 atm, and the pressure of the target was $\sim$6.5 atm. Recent tests from S. Christo (JLab) demonstrated the feasibility of a 3 atm target with a 30 μm wall, including safety margins.

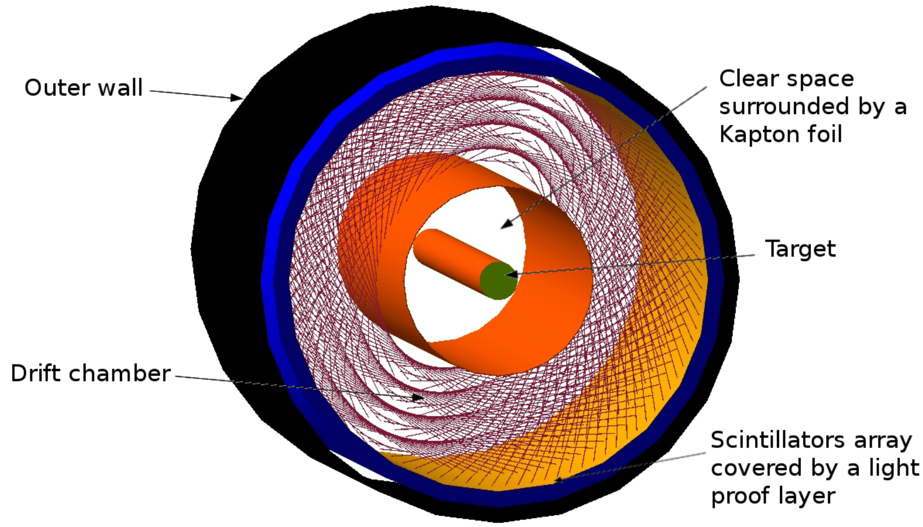

Figure 2.2: The schematic layout of the new recoil detector design, viewed from the beam direction.

2.2.1 Drift chamber

While drift chambers are very useful to cover large areas at a moderate price, huge progress has been made in terms of the ability to withstand higher rates using better electronics, shorter distance between wires and optimization of the electric field over pressure ratio. Our design is based on other chambers developed recently. For example for the dimuon arm of ALICE at CERN, drift chambers with cathode planes were built in Orsay [54]. The gap between sense wires is 2.1 mm and the distance between two cathode planes is also 2.1 mm, the wires are stretched over about 1 m. Belle II is building a cylindrical drift chamber very similar to what is needed for this experiment for which the space between wires is around 2.5 mm [55]. Finally, a drift chamber with wires gaps of 1 mm is being built for the small wheel of ATLAS at CERN [56]. The cylindrical drift chamber proposed for our experiment is 300 mm long, and we therefore considered that a 2 mm gap between wires was technically a rather conservative goal. Optimization is envisaged in the future based on experience with prototypes.

However, the radial form of the detector does not allow for 90 degrees x-y wires in the chamber. Thus, the wires of each layer are at alternating angles of $\pm$ 10°, called stereo-angle, from the axis of the drift chamber. We use a stereo angle between wires to determine the coordinate along the beam axis (z). It will make it possible to use a very thin forward end-plate to reduce multiple scattering of the outgoing high-energy electrons. A rough evaluation of the tension due to about 2600 of 300 mm long wires is under 600 kg, which appears to be reasonable for a composite endplate.

Our drift chamber cells are composed of one sense wire made of gold plated tungsten

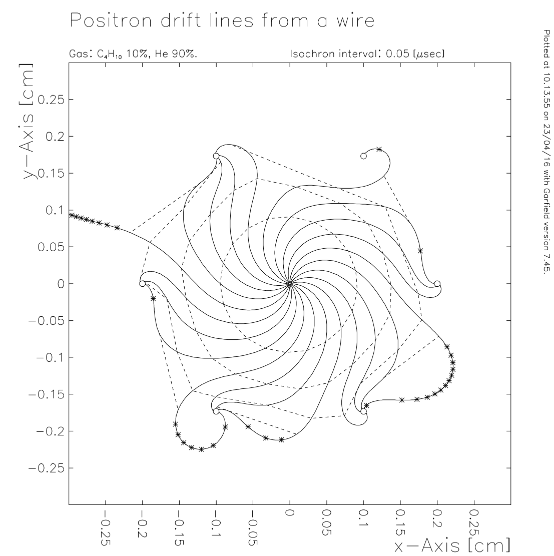

Figure 2.3: Drift lines simulated using MAGBOLTZ [57] for one sense wire (at the center) surrounded by 6 field wires. The two electric field lines leaving the cell disappear when adjusting the voltages on the wires. Dashed lines are isochrones spaced by 50 ns. It shows that the maximum drift time is about 250 ns.

surrounded by field wires, however the presence of the 5 T magnetic field complicates the field lines. Several structures have been studied with MAGBOLTZ [57] and will be tested in a prototype (see section 2.4). For now, we decided to choose a conservative configuration as shown in Fig. 2.3. The sense wire is surrounded by 6 field wires placed equidistantly from it in a hexagonal pattern. The distance between the sense and field wires is constant and equal to 2 mm. Two adjacent cells share the field wire placed between them. We plan 8 layers of cells at increasing radius from the target.

The simulation code MAGBOLTZ is calculating the drift speed and drift paths of the electrons (Fig. 2.3). With a moderate electric field, the drift speed is around 10 microns/ns, the average drift time expected is thus 250 ns (over 2 mm). Assuming a conservative 10 ns time resolution, the spatial resolution is expected to be around 200 microns due to field distortions and spread of the signal.

The maximum rates for protons are expected to be around 5 MHz for $2 \cdot 10^{34}$ cm^{-2}s^{-1}, for an integration time of 200 ns and considering 8 layers of sense wires where two readout wires

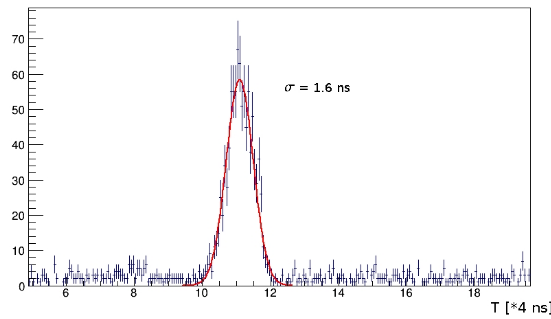

Figure 2.4: Typical time resolution of a crystal for HPS calorimeter.

are about 4 mm distant, the occupancy for the inner most layer is expected to be around 2 % which should be reasonable for a good tracking. When running coherent processes with the ^{4}He target, it is not necessary to detect the protons, and the rate can then be highly reduced by increasing the threshold, thus making the chamber blind to protons[2].

We are currently investigating two options to read out the signals from the wires. The first option would be to use the same preamplifier as the one developed for the CLAS inner calorimeter and improved for the Heavy Photon Search [58] experiment installed in Hall B. Depending on the gain in the drift chamber and the number of primary ionizations, it is possible to tune the gain of the preamplifier to adapt it to the needs of this experiment. More studies will be needed to evaluate how the gains of the chamber and the preamplifier can be tuned to ensure a noise that allows to select a threshold high enough to be blind to minimum ionizing particles. The time resolution of HPS has been shown to be around 1.6 ns for all crystals (Fig. 2.4) which is much better than our requirements.

The second option would be to use the electronics used by the Micromegas of CLAS12, known as the DREAM chip. Its dynamic range and time resolution seem to correspond to the need of our drift chamber. To ensure that it is the case, tests with a prototype will be performed (see section 2.4).

2.2.2 The scintillator array

The scintillator array will serve two main purposes. First, it will provide a useful complementary trigger signal because of its very fast response time, which will reduce the amount of random background triggers. Second, it will provide particle identification, primarily through a time-of-flight measurement, but also by a measurement of the particle total energy deposited and path length in the scintillator, the latter is important for doubly charged ions.

The length of the scintillators cannot exceed roughly 40 cm to keep the time resolution below 150 ps. It must also be segmented to match with tracks reconstructed in the drift

[2] The CLAS *eg6* run period was using the RTPC in the same fashion.

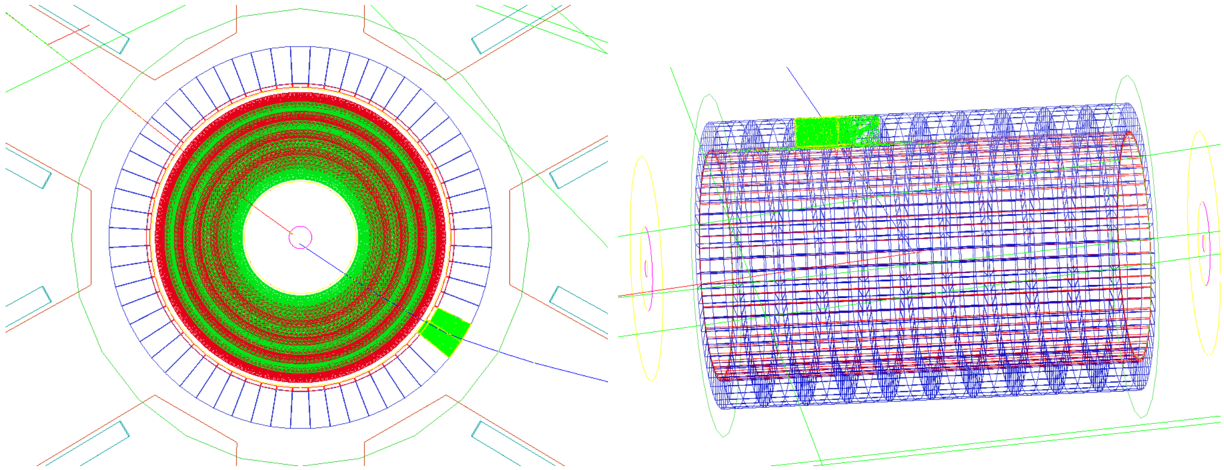

Figure 2.5: Geant4 simulation of a proton passing through the recoil drift chamber and scintillator hodoscope. The view looking downstream (left) shows the drift chamber's eight alternating layers of wires (green and red) surrounded by the two layers of scintillator (red and blue). Simulating a proton through the detector, photons (green) are produced in a few scintillators.

chamber. Since ^{3}He and ^{4}He will travel at most a few mm in the scintillator for the highest anticipated momenta (~ 400 MeV/c), a layered scintillator design provides an extra handle on particle identification by checking if the range exceeded the thickness of the first scintillator layer.

The initial scintillator design consists of a thin (2 mm) inner layer of 60 bars, 30 cm in length, and 600 segmented outer scintillators (10 segments 3 cm long for each inner bar) wrapped around the drift chamber. Each of these thin inner bar has SiPM detectors attached to both ends. A thicker outer layer (18 mm) will be further segmented along the beam axis to provide position information and maintain good time resolution.

For the outer layer, a dual ended bar design and a tile design with embedded WLS fiber readouts similar to the forward tagger's hodoscope for CLAS12 [59] were considered. After simulating these designs, it was found that the time resolution was insufficient except only for the smallest of tile designs ($15\times15\times7$ mm^3). Instead of using fibers, a SiPM will be mounted directly on the outer layer of a keystone shaped scintillator that is 30 mm in length and 18 mm thick. This design can be seen in Fig. 2.5 which shows a full Geant4 simulation of the drift chamber and scintillators.

The advantage of a dual ended readout is that the time sum is proportional to the TOF plus a constant. The improved separation of different particles can be seen in Fig. 2.6. Reconstructing the position of a hit along the length of a bar in the first layer is important for the doubly charged ions because they will not penetrate deep enough to reach the second layer of segmented scintillator.

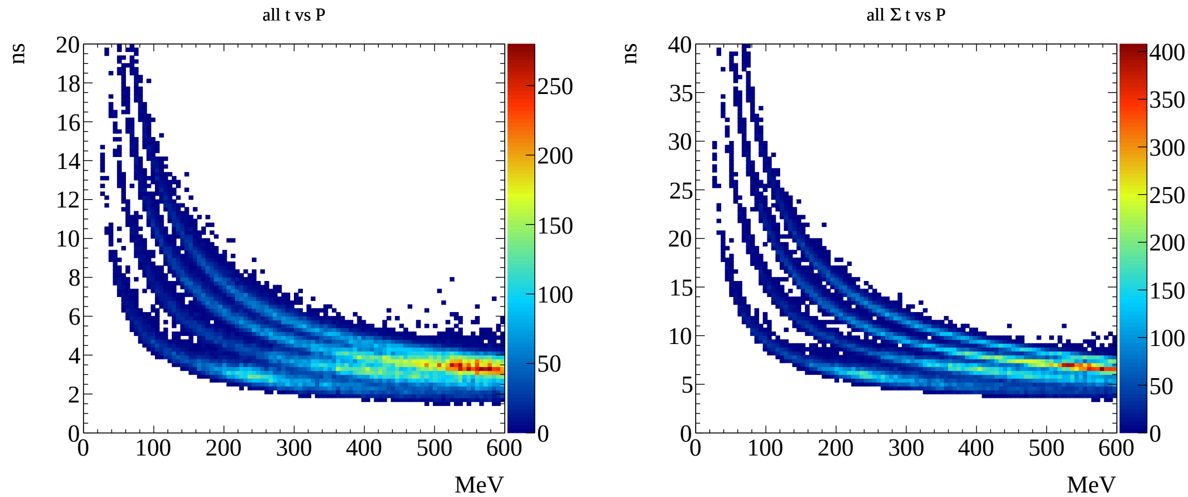

Figure 2.6: Simulated TOF for the various recoil particles vs Momentum. The TOF from just a single readout is shown on the left and the sum of the dual ended readout is shown on the right.

2.3 Reconstruction

The general detection and reconstruction scheme for ALERT is as follows. Fitting a track with the drift chamber and scintillator position information yields a track radius which is proportional to the momentum over the charge. Next, using the scintillator time-of-flight, the particles are separated and identified by ~~the~~ their mass-to-charge ratio, therefore leaving a degeneracy for the deuteron and α particles.

The degeneracy between deuteron and α particles can be lifted a few ways. The first and most simple way is to observe that an α will almost never make it to the second layer and therefore the absence (presence) of a signal would indicate the particle is an α(deuteron). Furthermore, as will be discussed below, the measured dE/dx will differ for ^{4}He and ^{2}H, therefore, taking into account energy loss in track fitting alone can provide separation. Additionally taking further advantage of the measured energy deposited in the scintillators can help separate the αs and deuterons.

In the studies we present here, we do not include ~~these~~ latter step. However, it is important to point out that extra information is available to us in form of energy deposited in both the drift chamber and the two scintillator layers. In a full reconstruction these will give extra constraints on the identification but also on the total momentum of the detected nucleus.

As ~~mentionned~~ earlier, we also want a DAQ trigger that is independent of the CLAS12 triggers ~~provided by ALERT~~. This trigger will be given by the scintillator signal, in coincidence with ~~signal~~ in a number of layers in the drift chamber. The exact number of drift chamber layers needed for the trigger, will be determined during the commissioning based on actual noise and occupancy levels.

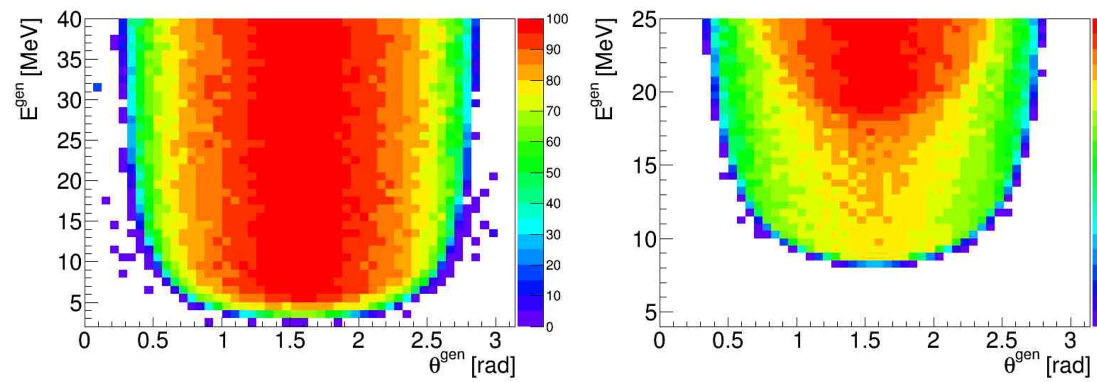

Figure 2.7: Simulated recoil detector acceptance, for protons (left) and ^{4}He (right), when requiring energy deposition in the scintillators array.

2.3.1 Track Fitting

The track obtained using a helix fit is used to determine the coordinates of the vertex point and the transverse momentum of the particle. The energy deposited in the scintillators can also be used to determine the kinetic energy of the nucleus. The feasibility and precision of the proposed vertex reconstruction and particle identification scheme were investigated with GEANT4 simulation.

The simulation of the recoil detector has been implemented with the full geometry and material specifications. It includes a 5 Tesla homogeneous solenoid field. The entire detector is filled with a very light gas mixture of He(90%) and C_4H_{10}(10%) set at atmospheric pressure to reduce energy loss and limit the energy deposition by minimum ionizing particles.

2.3.2 Track Reconstruction and Particle Identification

In the current study all recoil species are generated with the same distributions: flat in momentum from threshold up to 40 MeV ($\sim$ 250 MeV/c) for protons and about 25 MeV for other particles; isotropic angular coverage; flat distribution in z-vertex; and a radial vertex coordinate smeared around the beam line center by a Gaussian distribution of sigma equal the beam expectation radius (0.200 mm).

With the requirement that the particle reaches the scintillator and with a 30 cm length limit, there is a smoothly varying acceptance when averaged over the z-vertex position. This is shown from simulation in Fig. 2.7 for the lightest and heaviest recoil nuclei. However, this is a conservative estimate, since it only uses tracking information. A more elaborate PID scheme may be able to accommodate a larger acceptance for lower energy recoils.

First, the tracking capabilities of the recoil detector are investigated assuming a spatial resolutions of 200 μm for the drift chamber. The wires are strung in the z-direction with a stereo angle of 10°. For particles stopped in the scintillators, the resulting difference between

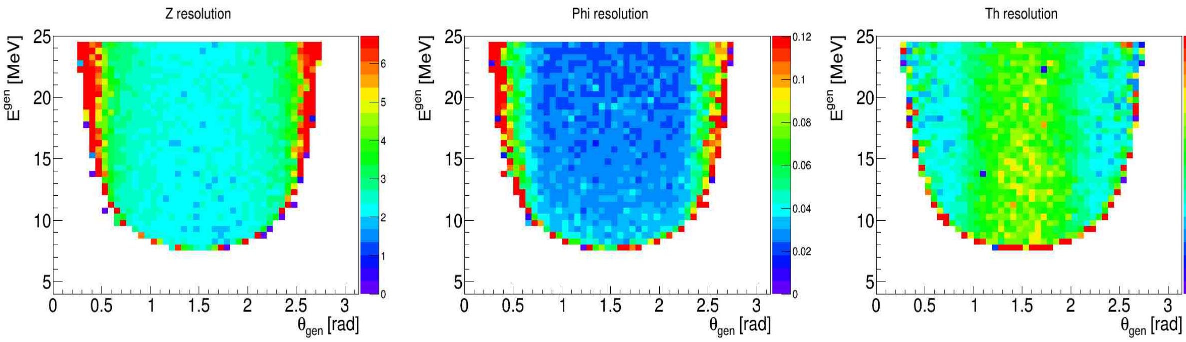

Figure 2.8: Simulated resolutions, integrated over z for ^{4}He, of the z-vertex (in mm) and the polar and azimuthal angles (in rad) for the lowest energy regime when the recoil track reaches the scintillator.

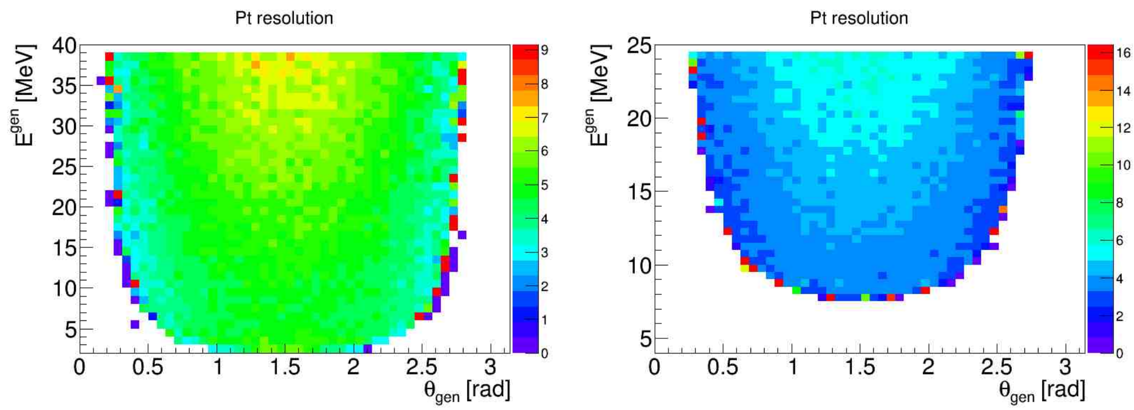

Figure 2.9: Simulated momentum resolutions for proton (left) and ^{4}He (right) integrated over z, when the recoil track reaches the scintillators array.

generated and reconstructed variables from simulation is shown in Fig. 2.8 for ^{4}He particles. The momentum for protons and ^{4}He was also reconstructed (Fig. 2.9) from the radius of the helix assuming a uniform 5 T field. From these plots, it is clear that the resolutions required are fulfilled.

Next, the particle identification scheme is investigated. The scintillators have been designed to ensure a 150 ps time resolution. To determine the dE/dx resolution measurements will be necessary for the scintillators and for the drift chamber as this depends on the detector layout, gas mixture, its electronics, voltages... Nevertheless, from [60], one can assume that with the 8 drift chamber measurements and the measurements in the scintillators, the energy resolution should be around 10% or better.

Under those conditions, a clean separation of three of the five nuclei is shown in Fig. 2.10 which represents the time of arrival in the scintillator as a function of the reconstructed

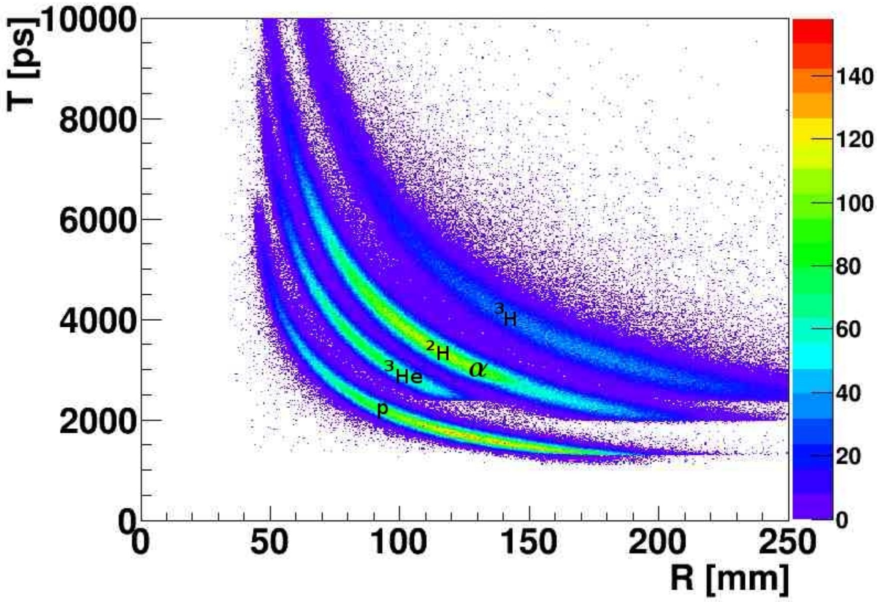

Figure 2.10: Simulated time of flight at the scintillator versus the reconstructed radius in the drift chamber. The bottom band corresponds to proton, next band is the ^{3}He nuclei, ^{2}H and α are overlapping in the third band, the uppermost band is ^{3}H. ^{2}H and α are separated using dE/dx.

radius in the drift chamber. ^{2}H from α are separated using dE/dx in the drift chamber and in the scintillators.

To quantify the separation power of our device, we simulated an equal quantity of each species. We obtained a particle identification efficiency of 99% for protons, 95% for ^{3}He and 98% for ^{3}H and around 90% for ^{2}H and α. It is important to note that for this analysis only the energy deposited in the scintillators was used, not the energy deposited in the drift chamber nor the path length in the scintillators, thus these ~~number~~ are very conservative. This analysis suggests that the proposed reconstruction and particle identification schemes for this design are quite promising. Studies, using both software and prototyping, are ongoing to determine the optimal detector parameters to minimize the detection threshold while maximizing particle identification efficiency. The resolutions presented above have been implemented in a fast Monte-Carlo used in the next section to evaluate the impact on our measurements.

2.4 Drift chamber prototype

Since the design of the drift chamber present several challenges, we decided ~~early~~ to build a prototype to investigate the feasibility of the project and start R&D projects in relation.

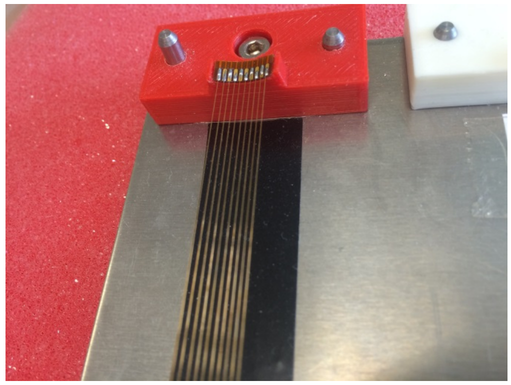

Figure 2.11: Welded wires on a curved structure with a 2 mm gap between each wire.

This section presents the work done in Orsay to address the main questions concerning the mechanics that needed to be answered:

- Can we build a stereo drift chamber with a 2 mm gap between wires?
- Can we design a frame that can be quickly changed in case of a broken wire?
- Can the forward structure be both light to reduce the multiple scattering and rigid enough to support the tension due to the wires?

For the first question, small plastic structures realized with a 3D printer were tested and wires welded on it. As shown in Fig. 2.11, it demonstrated our ability to weld wires with a 2 mm gap on a curved structure.

To limit issues linked to broken wires, we opted for a modular detector made of identical sectors. Each sector covers 20° of the azymuthal angle (Fig. 2.12) and can be rotated around the beam axis to be separated from the other sectors. This rotation is possible due to the absence of one sector, leaving a 20° dead angle. Then, if a wire breaks, its sector can be removed independently and replaced by a spare. Plastic and metallic prototype sectors were made with 3D printers to test the build-in procedure and we have started the construction of a full size prototype of one sector.

The shape of each sector is constrained by the position of the wires. It has a triangular shape on one side and due to the stereo angle the other side looks like a pine tree with branches alternatively going left and right from a central trunk (Fig. 2.13).

The last question about the light material will be studied in details with future prototypes. Nevertheless, current design plans are to use carbon in place of the aluminum in the forward region and titanium for the backward structure. The prototype was designed to check the mechanical requirements summarized above but also to verify the different cell configurations, and to test the DREAM electronics (time resolution, active range, noise). A total of five sectors have been build for tests, it will allow us to check that the elements can be properly

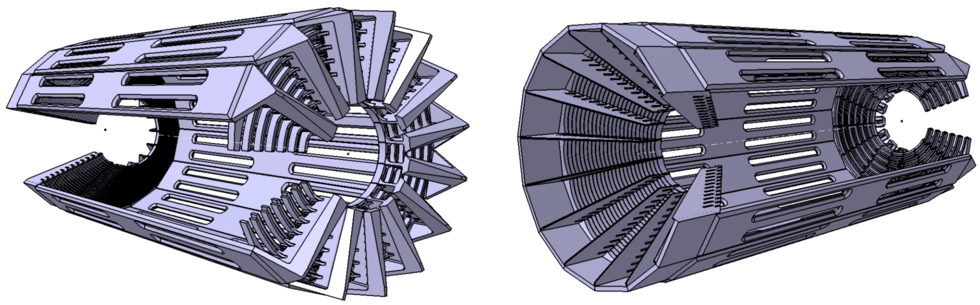

Figure 2.12: Backward (left) and forward (right) CAD of the prototype detector with all the sectors included.

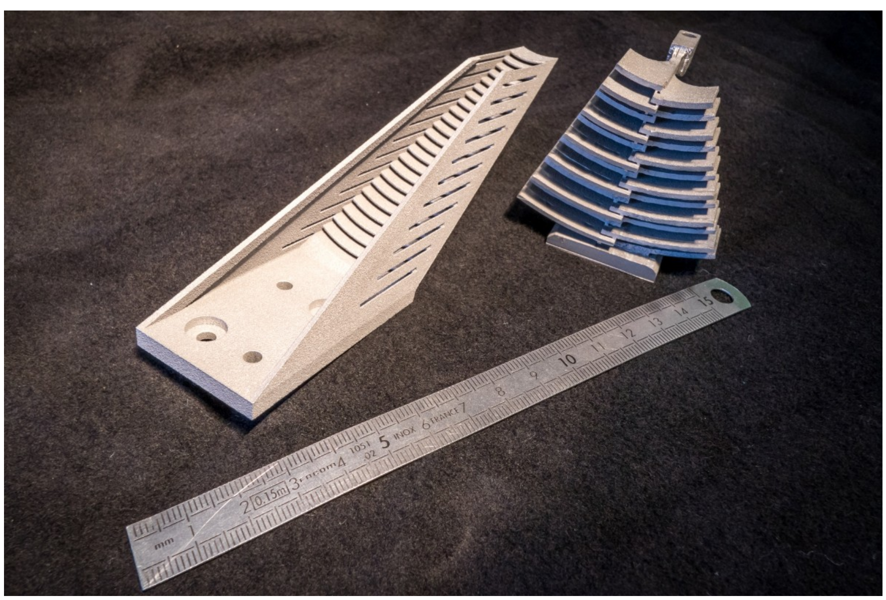

Figure 2.13: Mechanics of one sector for the prototype made with 3D printer.

positioned relatively to each other and one sector will be completely equipped with wires to be tested with a cosmic test bench and an α source.

2.5 Low Energy Recoil Detector

We explored other available solutions for the low-energy recoil tracker (ALERT) whth adequate momentum and spatial resolution, and good particle identification for recoiling light nuclei (p, ^{3}H and ^{3}He). After investigating the feasibility of the proposed measurements using the CLAS12 Central Detector and the BoNuS Detector [48, 44], we concluded that we needed to build a dedicated detector. We summarize in the following the elements that led us to this conclusion.

2.5.1 Central Detector

The CLAS12 Central Detector [53] is designed to detect various charged particles over a wide momentum and angular range. The main detector package includes:

- Solenoid Magnet: provides a central longitudinal magnetic field up to 5 Tesla, serves to curl emitted low energy Møller electrons and determine particle momenta through tracking.
- Central Tracker: consists of 3 layers of silicon strips and 3 layers of Micromegas. The thickness of a single silicon layer is 300μm.
- Central Time-of-Flight: an array of scintillator paddles with a cylindrical geometry of radius 26 cm and length 50 cm; the thickness of the detector is 2 cm with designed timing resolution of $\sigma_t = 50$ ps, used to separate pions and protons up to 1.2 GeV/c.

The current design, however, is not optimal for low energy particles ($p < 300$ MeV/c) due to the energy loss in the first 2 silicon strip layers. The momentum detection threshold is ~ 200 MeV/c for protons, ~ 350 MeV/c for deuterons and even higher for ^{3}H and ^{3}He. These values are significantly too large for our proposed measurements, therefore we needed to explore other detector options.

2.5.2 BoNuS12 Radial Time Projection Chamber

The original BoNuS detector was built for Hall B experiment E03-012 to study neutron structure at high x_B by scattering electrons off an almost on-shell neutron inside deuteron. The purpose of the detector was to tag the low energy recoil protons ($p > 60$ MeV/c). The key component for detecting the slow protons was the Radial Time Projection Chamber (RTPC) based on Gas Electron Multipliers (GEM). A later run period (EG6) used a ^{4}He gas target and a newly built and improved RTPC to detect recoiling α particles in coherent

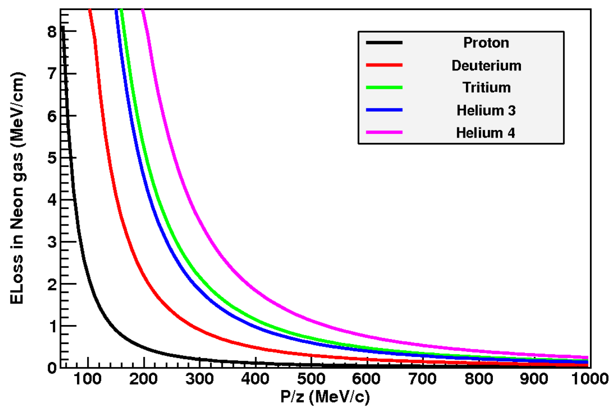

Figure 2.14: Calculation of energy loss in Neon gas as a function of the particle momentum divided by its charge for different nuclei.

DVCS scattering. The major improvements of the EG6 RTPC were full cylindrical coverage and a higher data taking rate.

The approved 12 GeV BoNuS (BoNuS12) proposal is planning to use a similar device with some upgrades. The target gas cell length will be doubled, and the new RTPC will be longer as well, leading to a doubling in luminosity and an increased acceptance. Taking advantage of the larger bore ($\sim$ 700 mm) of the 5 Tesla solenoid magnet, the maximum radial drift length will be increased from the present 3 cm to 4 cm, improving the momentum resolution by 50% [44] and extending the momentum coverage. The main features of the proposed BoNuS12 detector are summarized in Table 2.2.

In principle, particle identification can be obtained from the RTPC through the energy loss dE/dx in the detector as a function of the particle momentum (see Fig. 2.14). However, such a small difference between ^{3}H and ^{3}He makes impossible to discriminate them on an event by event basis because of the intrinsic width of the dE/dx distributions. This feature is not problematic when using the deuterium target, but makes the RTPC option not viable for our tagged EMC measurement on ^{4}He target.

Another issue with the RTPC is its slow response time due to the drift time ($\sim 5\mu$s). Indeed, a fast recoil detector could be included in the trigger and have significant impact on the background rejection. Indeed, in about 90% DIS on deuteron or helium the spectator fragments have too low energy or too small angle with the beam line to get out of the target to the detector. Since the data acquisition speed was the main limiting factor for both BoNuS and EG6 runs in CLAS, including the recoil detector in the trigger would allow us to run at higher luminosities. Indeed events without a hit in the recoil detector would not be recorded and this will significantly reduce the trigger's frequency.

Table 2.2: Comparison between the RTPC (left column) and the new tracker (right column).

Detectors	**RTPC**	**New Tracker**
Drift region radius	4 cm	5 cm
Longitudinal length	$\sim$ 40 cm	$\sim$ 40 cm
Gas mixture	80% helium/20% DME	90% helium/10% isobutane
Azimuthal coverage	360°	340°
Momentum range	70-250 MeV/c protons	70-250 MeV/c protons
Transverse mom. resolution	10% for 100 MeV/c protons	10% for 100 MeV/c protons
z resolution	3 mm	3 mm
Solenoidal field	$\sim$ 5 T	$\sim$ 5 T
ID all light nuclei	No	Yes
Trigger	can not be included	can be included

2.5.3 Need for a New Low Energy Recoil Detector

As explained in the previous sections, the threshold of the CLAS12 inner tracker is clearly too high to be used for our needs. On the other hand, the recoil detector planned for BoNuS12 and composed of a RTPC is not suitable due to its inability to distinguish all kind of particles required for our needs. Moreover, as the RTPC can not be efficiently included in the trigger, many background events are sent to the readout electronics, saturating it and limiting the maximum luminosity. Therefore, we propose to use A Low Energy Recoil Tracker (ALERT) based on a new detector design, described in the next section, that would provide good timing and energy loss information and a total energy measurement for each track. The fast timing will allow a tight time coincidence with CLAS12, thereby reducing the background that was encountered in previous RTPC detectors. The recoil detector can be included in the data acquisition trigger, which will largely reduce triggering on events from the target windows, which are outside the acceptance and events with recoil too slow to exit the target that cannot be used in the analysis.

Finally, the use of time of flight and dE/dx measurements will provide improved particle identification for the recoiling nuclei without ambiguity for ^{3}H and ^{3}He identification. The features and requirements for this new detector are compared with the current RTPC design for BoNuS12 in Table 2.2. The transverse momentum and z resolution are chosen following the BoNuS specifications.

2.6 Technical contributions from the research groups

2.6.1 Argonne National Laboratory

To be added

2.6.2 Institut de Physique Nucléaire d'Orsay

To be added

2.6.3 Jefferson Laboratory

To be added

2.6.4 Temple University

To be added

Chapter 3

Experimental reach

3.1 Proposed Measurements

In light of the physics motivation presented ~~above~~ and the ~~capabilities expected from~~ the new ALERT detector, we propose to measure the tagged deep-inelastic scattering off ^{2}H and ^{4}He from low to high momentum recoiling spectator ($70 < P_{A-1} < 400$ MeV/c). We choose the helium target for several reasons, first it is a light gas that can easily be used in a very light gaseous target allowing to detect very low momentum spectators. Also, calculation for FSI are theoretically very challenging, keeping the number of nucleon low is therefore of great help; moreover, as ~~A-1 spectator~~ get heavier, their detection threshold goes up such that we want to keep our target at low A. The reactions we are going to study are:

- $^2\mathrm{H}(e, e'p)X$ — bound neutron;
- $^4\mathrm{He}(e, e'\ ^3\mathrm{H})X$ — bound proton;
- $^4\mathrm{He}(e, e'\ ^3\mathrm{He})X$ — bound neutron;

3.1.1 Monte-Carlo Simulation

To estimate the rates of our experiment and provide meaningful estimates of our statistical error bars, we developed a Monte-Carlo simulation based on PYTHIA with some basic nuclear effects. The interaction on the nucleon is generated in a basic impulse approximation, neglecting the virtuality of the target nucleon. We simulate the Fermi motion of the nucleons in the target nuclei according to the distribution provided by AV18+UIX potentials [61, 62, 63]. This leads to a target nucleon with momentum $\vec{p}_n$, the nuclear spectator is generated with a kinematic opposite to the interacting nucleon, -$\vec{p}_n$. The PYTHIA Monte-Carlo provides simulation for the DIS interaction and the fragmentation of the partons, we do not include nuclear effects such as FSI here.

In the simulation, we select DIS by requesting $Q^2 > 1.5$ GeV^2 and $W > 2$ GeV. These are the same for all figures, indication on the figures are for the theoretical predictions. In our experimental configuration and with the cut described above, we expect $\langle Q^2 \rangle \sim 3$ GeV^2.

The generated final-state particles go through acceptance tests. Electrons, which will be detected by the forward detector, are treated by a GEANT4 Monte-Carlo simulation of CLAS12. The recoiling nuclei (including protons) acceptance is based on the GEANT4 simulation described in section 2.3 and represented in Fig. 2.7. On top of these estimates, we apply an overall 75% efficiency to this detection settings to account for the fiducial cuts and detector inefficiencies.

3.1.2 Beam Time Request

We estimate, based on past measurements with CLAS, that the ratios we want to measure will be affected by systematic errors of ~ 3 percents. Our beam time request, allows to have the statistical error bars of our key measurement (Fig. 3.3 right) at the same level. Assuming ~~the~~ luminosity of 2.10^{34} cm^2.s^{-1}, this method drive to a request of 30 days for each target.

Another constrain is the demands of the other proposals of the run group. In particular, as the deeply virtual Compton scattering (DVCS) cross section is very small, the helium GPD proposal will need more running time. It has been evaluated to 60 days in the dedicated proposal, we therefore present below projections including the full run group beam time request of 60+30 days.

3.2 Projections

Based on our simulation, we determine the available kinematic range and production rates accessible for each channel. The x_B and recoil momenta distributions are illustrated in Fig. 3.1 for tagged ^3H out of an ^{4}He target, this figure shows the available phase space for a measurement of the bound proton structure function.

3.2.1 Testing the Spectator Model

The projections presented in Fig. 3.2 show the capability of this experiment to measure cross section ratios of DIS on a bound nucleon in light nuclei and, therefore, our capability to check the validity of the spectator model used by the theoretical predictions. Statistical error bars in this figure are very modest and even smaller than the points on the logarithmic scale. It is therefore clear that we have capability to test the spectator model in detail.

The high precision we can obtain for this channel should lead to more valuable confirmation of assumptions made for other similar measurements, such as BoNuS. We will be able to carry out, multi-dimensional test for the FSI models as was done in [65] and for the first time make such study on helium. Other tests have been proposed to insure that outgoing pions are formed far enough from the nuclei to limit FSI [66, 67] and understand the color

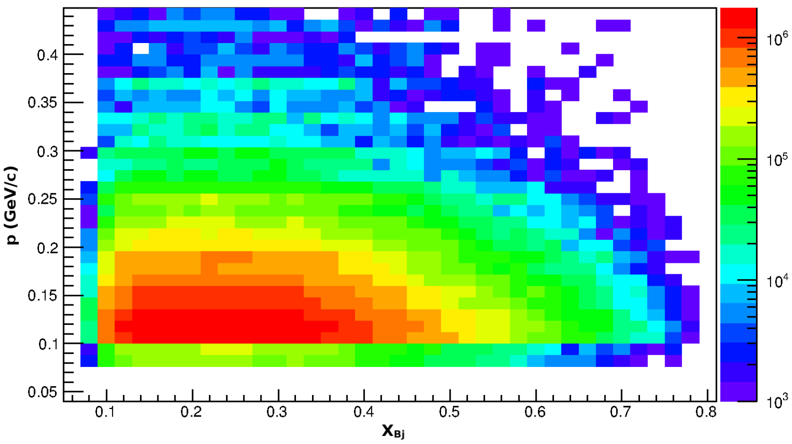

Figure 3.1: Expected event count as a function of x_B and the recoil momentum of the ^{3}H from a ^{4}He target.

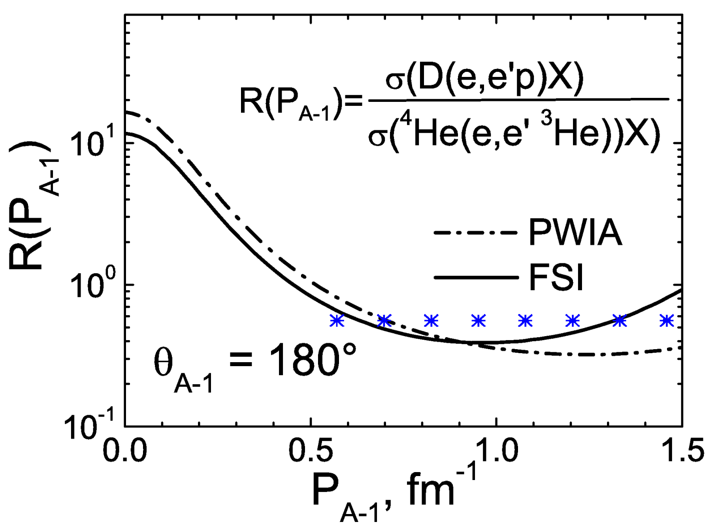

Figure 3.2: This figure is similar to ~~figure~~ 1.2, it shows the predictions for CLAS12 kinematic [24, 64] of the ratio $R(^4\text{He}, ^2\text{H}, |\vec{P}_{A-1}|)$ compared to projected statistical error bars for the proposed experiment (blue points).

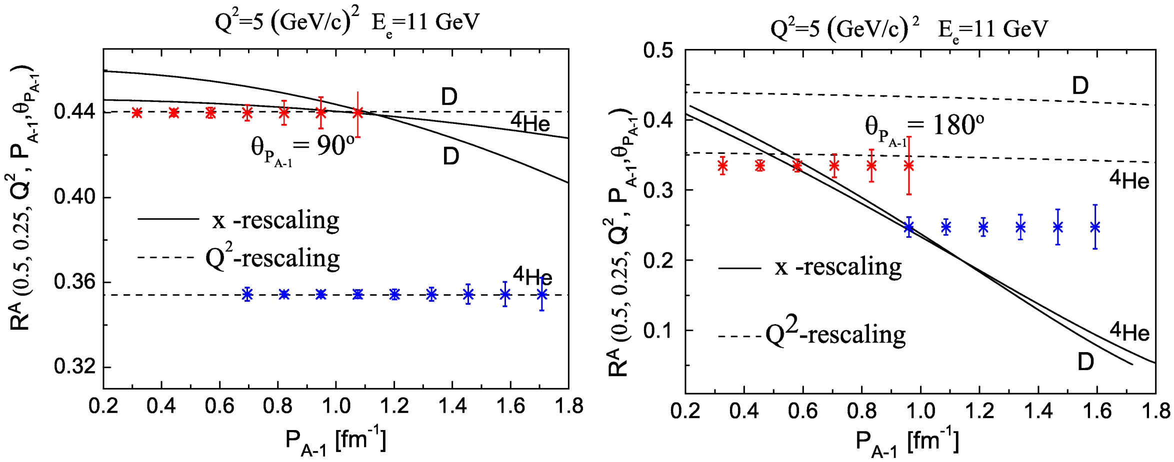

Figure 3.3: This figure is similar to ~~figure~~ 1.4, it shows predictions of the ratio $R^A(x, x')$ for $A = 2$ and $A = 4$ as a function of the momentum of the recoil nucleus $A-1$ at perpendicular (left) and backward (right) angle. The full and dashed curves are predictions for CLAS12 kinematic [24, 64] of the x-rescaling (binding) and Q^2-rescaling models, respectively, points are projections for ^{2}H (red) and ^{4}He (blue).

transparency effect associated. This study is most sensitive to spectators emitted at 90°, where the effect is larger, and can then be extrapolated to lower angles. In [50], testing that the x_B scaling holds in tagged DIS is proposed as another way to confirm the soundness of the procedure.

Thanks to its high statistics, the experiment will therefore have the possibility to make thorough test of the spectator mechanism and its limits. In particular it will for the first time experimentally explore this framework for $A > 2$, opening completely new opportunities for light nuclei tagged experiments.

3.2.2 EMC effect in deuterium

To be added

3.2.3 Testing the Rescaling Models

The main goal of our experiment is to discriminate decisively between models of EMC, Fig. 3.3 illustrates this capability. We have here a high differentiation power between x-rescaling and Q^2-rescaling models. We note the good coverage and small error bars for $\theta_{P_{A-1}} = 90°$ ($75 < \theta_{P_{A-1}} < 105°$), this is due to the better acceptance for this angle. The measurement at backward angle ($\theta_{P_{A-1}} > 150°$), however, is much more difficult and is the main constraint driving our beam time request. Still, in order to obtain acceptable error bars

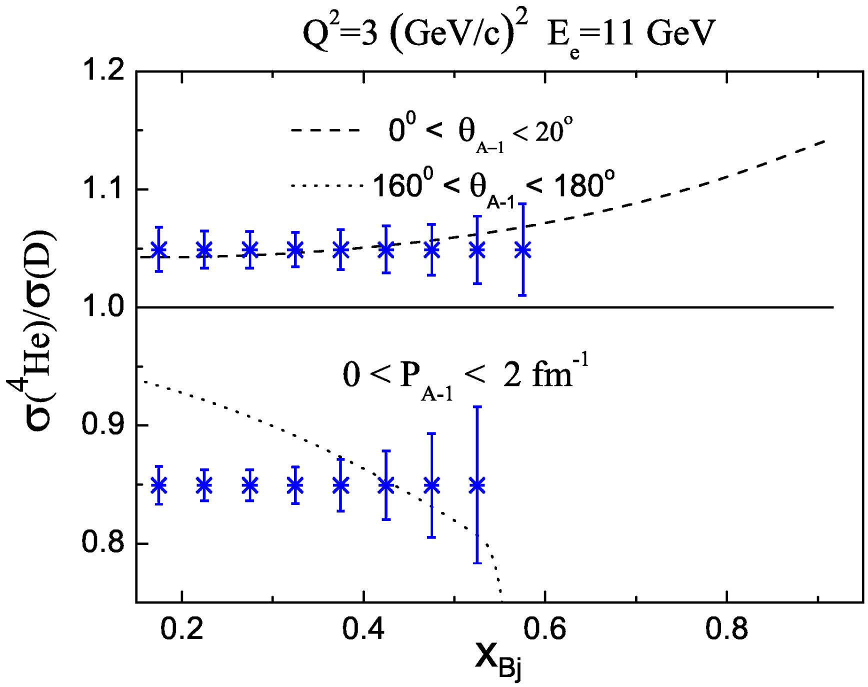

Figure 3.4: This figure is similar to ~~figure~~ 1.5, it shows the semi-inclusive EMC ratio $R_0(x, Q^2)$ as a function of x_B with recoils emitted forward and backward, the dashed and dotted curves are predictions for the local EMC effect for CLAS12 kinematic [24, 64] the blue points are statistical error bar projections for our measurement.

with a reasonable beam time request, the backward ~~angle~~ are selected up to 150° instead of the 160° for the theory predictions.

We notice a complementarity between the target in the phase space covered, this is due to the fact that larger recoil nuclei are more absorbed by the target material and have higher detection threshold. At the same time, the Fermi momentum is larger in helium allowing better statistics at high p_{A-1}. Using helium is then also an opportunity to explore higher spectator momentum with a reasonable amount of beam time.

3.2.4 Tagged EMC Ratio

The experiment can also confront the striking predictions for backward versus forward tagged EMC in binding models, as illustrated in the Fig. 3.4. We see that the model prediction will be clearly tested, however the reach in x_B for the backward recoils is also an important ~~constrain~~ on the beam time needed by the experiment. Indeed, the strongest effect is expected at $x_B \sim 0.5$ and necessitates high statistics.

The measurement of the tagged EMC ratio is a very clean observable even for other kinds of ~~model~~, in the low momentum regime one should be able to reproduce very nicely the classic

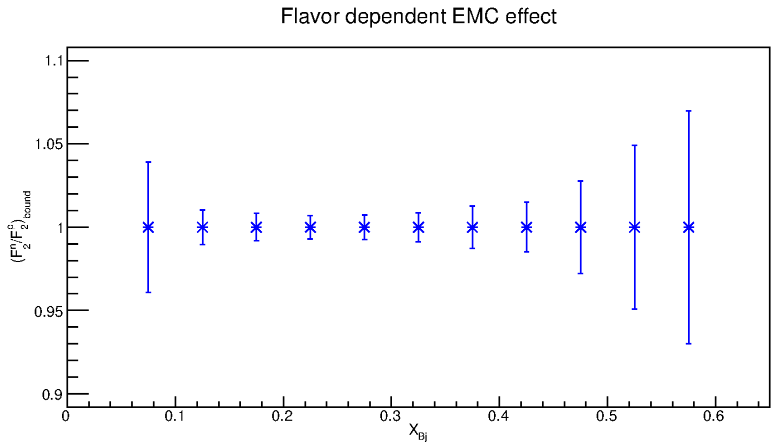

Figure 3.5: Statistical error bar projections for the ratio F_2^n/F_2^p for bound nucleons as a function of x_{Bj} using an ^{4}He target.

EMC effect and then be able to study its dependence ~~with~~ spectator angle and momentum. As was shown before, the different models offer very different expectations, in particular, models only based on virtuality ~~should~~ give a ratio of 1 when we select the same spectator kinematic.

3.2.5 ~~Measuring~~ the Flavor Dependent Nuclear Effects

Finally with our setup, we ~~can~~ explore the flavor dependence of nuclear PDFs. Figure 3.5 illustrates our capabilities, ~~theoretical predictions~~ for ^{4}He in the isovector model is 1 [52], but others predict that nuclear effects change the d/u ratio and should therefore be observed here [51]. We will be able to explore any variation in bound nucleons with ~~1-2%~~ statistical error bars – *i.e.* 4% when including expected systematic error bars – from x_B of 0.1 to 0.5.

Summary and Beam Time Request

In summary, we proposed a tagged DIS measurement on light nuclear targets (D and ^{4}He) by detecting the backward recoiling spectator. By taking the advantage of the high luminosity and large kinematic coverage of CLAS12, we will be able to cover a wide range in spectator kinematic insuring a good control over FSI effects.

In order to make this measurement, we propose to use a new low momentum recoil detector to fit our experimental needs in term of slow nuclei detection. The detector is designed such that it will provide good timing resolution and particle identification. Prototyping of this detector is already ongoing in Orsay as part of a larger R&D program on drift chambers.

We propose to measure various tagged ratios and double ratios with their dependence on the recoil kinematics. These measurements will provide very stringent tests of numerous models for the EMC and anti-shadowing effects and, more importantly, a model independent insight into the origin of the EMC effect in term of x_B or Q^2-rescaling.

In order to achieve all the goals presented in this proposal, we need 60 days of running with an 11 GeV electron beam at 2.10^{34} cm^2.s^{-1} (= 150 nA) with helium and deuterium targets (30 days each) and 10 days of commissioning of the ALERT detector at 11 GeV and 2.2 GeV (5 days each) and various luminosities with helium and hydrogen targets.

Bibliography

[1] J. J. Aubert *et al.*, "The ratio of the nucleon structure functions $F2_n$ for iron and deuterium," *Phys. Lett.*, vol. B123, pp. 275–278, 1983.

[2] J. Ashman *et al.*, "Measurement of the Ratios of Deep Inelastic Muon - Nucleus Cross-Sections on Various Nuclei Compared to Deuterium," *Phys.Lett.*, vol. B202, p. 603, 1988.

[3] M. Arneodo *et al.*, "Shadowing in Deep Inelastic Muon Scattering from Nuclear Targets," *Phys.Lett.*, vol. B211, p. 493, 1988.

[4] M. Arneodo *et al.*, "Measurements of the nucleon structure function in the range $0.002-\mathrm{GeV}^2 < x < 0.17-\mathrm{GeV}^2$ and $0.2-GeV^2 < q^2 < 8-GeV^2$ in deuterium, carbon and calcium," *Nucl.Phys.*, vol. B333, p. 1, 1990.

[5] J. Gomez *et al.*, "Measurement of the A-dependence of deep inelastic electron scattering," *Phys.Rev.*, vol. D49, pp. 4348–4372, 1994.

[6] D. Allasia *et al.*, "Measurement of the neutron and the proton F2 structure function ratio," *Phys.Lett.*, vol. B249, pp. 366–372, 1990.

[7] J. Seely *et al.*, "New measurements of the EMC effect in very light nuclei," *Phys. Rev. Lett.*, vol. 103, p. 202301, 2009.

[8] D. F. Geesaman, K. Saito, and A. W. Thomas, "The nuclear EMC effect," *Ann. Rev. Nucl. Part. Sci.*, vol. 45, pp. 337–390, 1995.

[9] P. R. Norton, "The EMC effect," *Rept. Prog. Phys.*, vol. 66, pp. 1253–1297, 2003.

[10] S. Malace, D. Gaskell, D. W. Higinbotham, and I. Cloet, "The Challenge of the EMC Effect: existing data and future directions," *Int.J.Mod.Phys.*, vol. E23, p. 1430013, 2014.

[11] M. Ericson and A. W. Thomas, "Pionic Corrections and the EMC Enhancement of the Sea in Iron," *Phys. Lett.*, vol. B128, p. 112, 1983.

[12] G. V. Dunne and A. W. Thomas, "DEEP INELASTIC SCATTERING AS A PROBE OF NUCLEON AND NUCLEAR STRUCTURE," *Nucl. Phys.*, vol. A446, pp. 437c–443c, 1985.

[13] S. V. Akulinichev, S. A. Kulagin, and G. M. Vagradov, "The Role of Nuclear Binding in Deep Inelastic Lepton Nucleon Scattering," *Phys. Lett.*, vol. B158, pp. 485–488, 1985.

[14] H. Jung and G. A. Miller, "NUCLEONIC CONTRIBUTION TO LEPTON NUCLEUS DEEP INELASTIC SCATTERING," *Phys. Lett.*, vol. B200, pp. 351–356, 1988.

[15] F. E. Close, R. G. Roberts, and G. G. Ross, "The Effect of Confinement Size on Nuclear Structure Functions," *Phys. Lett.*, vol. B129, p. 346, 1983.

[16] O. Nachtmann and H. J. Pirner, "COLOR CONDUCTIVITY IN NUCLEI AND THE EMC EFFECT," *Z. Phys.*, vol. C21, p. 277, 1984.

[17] R. L. Jaffe, F. E. Close, R. G. Roberts, and G. G. Ross, "On the Nuclear Dependence of Electroproduction," *Phys. Lett.*, vol. B134, p. 449, 1984.

[18] F. E. Close, R. G. Roberts, and G. G. Ross, "FACTORIZATION SCALE INDEPENDENCE, THE CONNECTION BETWEEN ALTERNATIVE EXPLANATIONS OF THE EMC EFFECT AND QCD PREDICTIONS FOR NUCLEAR PROPERTIES," *Nucl. Phys.*, vol. B296, p. 582, 1988.

[19] L. Frankfurt and M. Strikman, "POINT - LIKE CONFIGURATIONS IN HADRONS AND NUCLEI AND DEEP INELASTIC REACTIONS WITH LEPTONS: EMC AND EMC LIKE EFFECTS," *Nucl.Phys.*, vol. B250, pp. 143–176, 1985.

[20] K. Ackerstaff *et al.*, "Nuclear effects on R = sigma(L)/sigma(T) in deep inelastic scattering," *Phys. Lett.*, vol. B475, pp. 386–394, 2000.

[21] L. Frankfurt and M. Strikman, "High-Energy Phenomena, Short Range Nuclear Structure and QCD," *Phys.Rept.*, vol. 76, pp. 215–347, 1981.

[22] S. Kumano and F. E. Close, "DEPENDENCE OF THE EMC EFFECT ON NUCLEAR STRUCTURE," *Phys. Rev.*, vol. C41, pp. 1855–1858, 1990.

[23] C. Ciofi degli Atti and S. Liuti, "Can nuclear binding explain the classical EMC effect?," *Nucl.Phys.*, vol. A532, pp. 241–248, 1991.

[24] C. Ciofi degli Atti, L. P. Kaptari, and S. Scopetta, "Semi-inclusive deep inelastic lepton scattering off complex nuclei," *Eur. Phys. J.*, vol. A5, pp. 191–207, 1999.

[25] D. Higinbotham, J. Gomez, and E. Piasetzky, "Nuclear Scaling and the EMC Effect," 2010.

[26] L. Weinstein *et al.*, "Short Range Correlations and the EMC Effect," *Phys.Rev.Lett.*, vol. 106, p. 052301, 2011.

[27] L. Frankfurt, M. Strikman, D. Day, and M. Sargsian, "Evidence for short range correlations from high Q**2 (e, e-prime) reactions," *Phys.Rev.*, vol. C48, pp. 2451–2461, 1993.

[28] K. Egiyan *et al.*, "Observation of nuclear scaling in the A(e, e-prime) reaction at x(B) greater than 1," *Phys.Rev.*, vol. C68, p. 014313, 2003.

[29] K. Egiyan *et al.*, "Measurement of 2- and 3-nucleon short range correlation probabilities in nuclei," *Phys.Rev.Lett.*, vol. 96, p. 082501, 2006.

[30] O. Hen *et al.*, "Momentum sharing in imbalanced Fermi systems," *Science*, vol. 346, pp. 614–617, 2014.

[31] C. Ciofi degli Atti *et al.*, "On the dependence of the wave function of a bound nucleon on its momentum and the EMC effect," *Phys. Rev.*, vol. C76, p. 055206, 2007.

[32] N. Baillie *et al.*, "Measurement of the neutron F2 structure function via spectator tagging with CLAS," *Phys.Rev.Lett.*, vol. 108, p. 142001, 2012.

[33] M. Hattawy *et al.* (EG6 Working Group), "Deeply Virtual Compton Scattering off ^{4}He," *CLAS internal analysis note*, 2016.

[34] C. Ciofi degli Atti and B. Z. Kopeliovich, "Final state interaction in semi-inclusive DIS off nuclei," *Eur. Phys. J.*, vol. A17, pp. 133–144, 2003.

[35] C. Ciofi degli Atti, L. Kaptari, and B. Kopeliovich, "Final state interaction effects in semiinclusive DIS off the deuteron," *Eur.Phys.J.*, vol. A19, pp. 145–151, 2004.

[36] M. Alvioli, C. Ciofi degli Atti, and V. Palli, "Slow proton production in semi-inclusive DIS off nuclei: The Role of final state interaction," *Nucl.Phys.*, vol. A782, pp. 175–178, 2007.

[37] V. Palli *et al.*, "Slow Proton Production in Semi-Inclusive Deep Inelastic Scattering off Deuteron and Complex Nuclei: Hadronization and Final State Interaction Effects," *Phys.Rev.*, vol. C80, p. 054610, 2009.

[38] L. Frankfurt and M. Strikman, "Hard Nuclear Processes and Microscopic Nuclear Structure," *Phys.Rept.*, vol. 160, pp. 235–427, 1988.

[39] C. Ciofi degli Atti and S. Simula, "Slow proton production in semiinclusive deep inelastic lepton scattering off nuclei," *Phys.Lett.*, vol. B319, pp. 23–28, 1993.

[40] W. Melnitchouk, M. Sargsian, and M. I. Strikman, "Probing the origin of the EMC effect via tagged structure functions of the deuteron," *Z. Phys.*, vol. A359, pp. 99–109, 1997.

[41] C. Ciofi delgi Atti and L. Kaptari, "A Non factorized calculation of the process He-3(e,e-prime p) H-2 at medium energies," *Phys.Rev.Lett.*, vol. 100, p. 122301, 2008.

[42] C. Ciofi degli Atti and L. Kaptari, "Semi-inclusive Deep Inelastic Scattering off Few-Nucleon Systems: Tagging the EMC Effect and Hadronization Mechanisms with Detection of Slow Recoiling Nuclei," *Phys.Rev.*, vol. C83, p. 044602, 2011.

[43] W. Melnitchouk, A. W. Schreiber, and A. W. Thomas, "Deep inelastic scattering from off-shell nucleons," *Phys. Rev.*, vol. D49, pp. 1183–1198, 1994.

[44] M. Amarian *et al.*, "The Structure of the Free Neutron at Large x-Bjorken (PR12-06-113)," *A proposal to PAC 30*, 2006.

[45] O. Hen *et al.*, "In Medium Nucleon Structure Functions, SRC, and the EMC effect (PR12-11-107)," *A proposal to PAC 38*, 2011.

[46] O. Hen *et al.*, "In Medium Nucleon Structure Functions, SRC, and the EMC effect (PR12-11-003A)," *A run group proposal to PAC 43*, 2015.

[47] A. Klimenko *et al.*, "Electron scattering from high-momentum neutrons in deuterium," *Phys.Rev.*, vol. C73, p. 035212, 2006.

[48] H. Fenker *et al.*, "BoNus: Development and use of a radial TPC using cylindrical GEMs," *Nucl. Instrum. Meth.*, vol. A592, pp. 273–286, 2008.

[49] M. Sargsian and M. Strikman, "Model independent method for determination of the DIS structure of free neutron," *Phys. Lett.*, vol. B639, pp. 223–231, 2006.

[50] W. Cosyn, V. Guzey, M. Sargsian, M. Strikman, and C. Weiss, "Electron-deuteron DIS with spectator tagging at EIC: Development of theoretical framework," *EPJ Web Conf.*, vol. 112, p. 01022, 2016.

[51] S. J. Brodsky, I. Schmidt, and J.-J. Yang, "Nuclear antishadowing in neutrino deep inelastic scattering," *Phys. Rev.*, vol. D70, p. 116003, 2004.

[52] I. C. Cloet, W. Bentz, and A. W. Thomas, "Isovector EMC effect explains the NuTeV anomaly," *Phys. Rev. Lett.*, vol. 102, p. 252301, 2009.

[53] "CLAS12 Technical Design Report," 2008.

[54] J. Peyré, B. Genolini, and J. Poutas, "A Full-Scale Prototype for the Tracking Chambers of the ALICE Muon Spectrometer," 1998.

[55] T. Abe *et al.*, "Belle II Technical Design Report," 2010.

[56] E. Etzion *et al.*, "The Certification of ATLAS Thin Gap Chambers Produced in Israel and China," 2004.

[57] S. Biagi, "Monte Carlo simulation of electron drift and diffusion in counting gases under the influence of electric and magnetic fields," *Nucl.Instrum.Meth.*, vol. A421, pp. 234–240, 1999.

[58] M. Battaglieri *et al.*, "The Heavy Photon Search test detector," *Nucl.Instrum.Meth.*, vol. A777, pp. 91–101, 2015.

[59] T. C. Collaboration, "Clas12 forward tagger (ft) technical design report." `https://www.jlab.org/Hall-B/clas12-web/docs/ft-tdr.2.0.pdf`, 2012. Online; accessed 29 January 2016.

[60] K. Emi *et al.*, "Study of a dE/ dx measurement and the gas-gain saturation by a prototype drift chamber for the BELLE-CDC," *Nucl. Instrum. Meth.*, vol. A379, pp. 225–231, 1996.

[61] R. B. Wiringa, V. Stoks, and R. Schiavilla, "An Accurate nucleon-nucleon potential with charge independence breaking," *Phys.Rev.*, vol. C51, pp. 38–51, 1995.

[62] B. S. Pudliner *et al.*, "Quantum Monte Carlo calculations of nuclei with A ¡= 7," *Phys.Rev.*, vol. C56, pp. 1720–1750, 1997.

[63] R. B. Wiringa *, Private communication.*

[64] C. Ciofi degli Atti *, Private communication.*

[65] W. Cosyn and M. Sargsian, "Final-state interactions in semi-inclusive deep inelastic scattering off the Deuteron," *Phys. Rev.*, vol. C84, p. 014601, 2011.

[66] K. Egiian, L. Frankfurt, W. R. Greenberg, G. A. Miller, M. Sargsian, and M. Strikman, "Searching for color coherent effects at intermediate Q**2 via double scattering processes," *Nucl. Phys.*, vol. A580, pp. 365–382, 1994.

[67] L. L. Frankfurt, W. R. Greenberg, G. A. Miller, M. M. Sargsian, and M. I. Strikman, "Color transparency effects in electron deuteron interactions at intermediate Q**2," *Z. Phys.*, vol. A352, pp. 97–113, 1995.